Ecological Modelling 516 (2026) 111546

Contents lists available at ScienceDirect

Ecological Modelling

journal homepage: www.elsevier.com/locate/ecolmodel

Physiologically-based eco-epidemiological model of *Xylella fastidiosa* infection in olive groves

Igor Daniel Weber [a], Anna Simonetto [a,*], Enrico Bertoldi [a], Paola Gervasio [a], Maria Saponari [b], Crescenza Dongiovanni [c], Juan Antonio Navas-Cortés [d], Gianni Gilioli [a]

[a] Università di Brescia, Via Branze 43, Brescia 25123, Italy
[b] Institute for Sustainable Plant Protection, National Research Council (CNR), Bari 70126, Italy
[c] Centro di Ricerca, Formazione e Sperimentazione in Agricoltura "Basile Caramia" (CRSFA), Locorotondo, Bari 70010, Italy
[d] Institute for Sustainable Agriculture (IAS), Spanish National Research Council (CSIC), Avda. Menéndez Pidal s/n, Córdoba 14004, Spain

ARTICLE INFO

Keywords:
Vector-borne plant disease
Insect-plant interaction
Olive quick decline syndrome
Disease progression
Philaenus spumarius

ABSTRACT

Xylella fastidiosa (*Xf*) is a plant pathogen of global concern, responsible for severe diseases in numerous crops, including Olive Quick Decline Syndrome (OQDS) in Europe. Understanding the eco-epidemiological processes governing the *Xf* infection and disease progression is essential for supporting the development of effective and sustainable management strategies against *Xf* outbreaks. We developed a novel physiologically based eco-epidemiological model to simulate *Xf* dynamics in olive agroecosystems. The model integrates vector population dynamics, vector–host interactions, transmission processes, disease progression in olive trees, explicitly accounting for the influence of temperature, water availability, and host plant composition. It is formulated as a system of ordinary and delay differential equations solved numerically, whose compartments represent vector life stages, herbaceous vegetation, non-host plants, reservoir plants, and successive olive tree disease stages defined by infection status and canopy desiccation severity. The model was calibrated and validated using field observations from 16 olive groves affected by *Xf* in Apulia (Italy), comparing simulated and observed distributions of olive trees across disease severity classes over time. Simulations successfully reproduced key epidemiological features, including the dynamics of disease severity classes, the duration of the asymptomatic period, the time from symptom onset to complete canopy desiccation, and the seasonal peaks in infected vector populations. This model advances our understanding of *Xf* epidemiology and provides a potential mechanistic tool to support pest risk assessment and integrated pest management by enabling scenario testing of disease spread and control strategies in olive-growing landscapes under different environmental conditions.

1. Introduction

Xylella fastidiosa (*Xf*) Wells (1987) (Proteobacteria: Xanthomonadaceae) is a xylem-limited, Gram-negative bacterium that infects over 700 plant species (EFSA, 2025). It is the causal agent of economically significant diseases, including Pierce's disease of grapevine, citrus variegated chlorosis, almond leaf scorch, and olive quick decline syndrome, and poses a substantial threat to agriculture worldwide (EFSA PLH Panel, 2019). The pathogenic process of *Xf* begins with the colonization of the xylem vessels of the host plants, where it progressively multiplies and spreads, inducing xylem occlusions (i.e., tyloses, callose-like structures, and gums/pectin gels) that impair plant hydraulic conductivity (Rapicavoli et al., 2018; Sicard et al., 2018; Sun et al., 2013). As a result, *Xf* infection induces primarily associated with water stress, such as marginal leaf necrosis and scorching, progressing to twigs and branch dieback until plant death (Rapicavoli et al., 2018). The successful establishment of infection and disease progression depends on multiple factors, such as pathogen genotype, host susceptibility, plant–pathogen interaction dynamics, environmental conditions (e.g., temperature, water availability), as well as vector population dynamics, abundance, dispersal capacity and transmission efficiency (Bodino et al., 2023; EFSA PLH Panel, 2019; Sicard et al., 2018).

Native to the Americas, *Xf* is currently present in Europe, Middle East and Asia. First severe European outbreak was documented in 2013, when *Xf* subsp. *pauca* triggered a devastating epidemic in olive groves in Apulia, Italy (Saponari et al., 2013, 2019). Since then, the three major *Xf*

* Corresponding author.
E-mail address: anna.simonetto@unibs.it (A. Simonetto).

https://doi.org/10.1016/j.ecolmodel.2026.111546
Received 17 October 2025; Received in revised form 21 February 2026; Accepted 26 February 2026

subspecies (*fastidiosa, multiplex*, and *pauca*) have been reported in several countries across Europe, where they have caused significant outbreaks in diverse agroecosystems (Schneider et al., 2020; Sicard et al., 2018). *Xf* is transmitted by xylem-feeding insects, with the spittlebug *Philaenus spumarius* L. (1758) (Hemiptera: Aphrophoridae) recognized as the primary vector in European outbreaks up to date (Cornara et al., 2018; EFSA PLH Panel, 2019). In the vector, the bacterium colonizes and multiplies in the foregut, enabling persistent transmission without a latency period (Almeida et al., 2005).

Several modelling frameworks have been developed to investigate the epidemiology of *Xf*. A common approach for analysing transmission processes between vectors and plants uses compartmental models, such as the Susceptible-Infected-Removed (SIR) framework (Soubeyrand et al., 2018) and extensions that incorporate temperature-dependent variables to predict the global distribution of *Xf* (Giménez-Romero et al., 2022). Some studies have further refined these models, e.g., Susceptible-Exposed-Infected-Removed (SEIR) models, by including host infection stages and explicitly accounting for an asymptomatic phase to better represent disease progression (Jeger and Bragard, 2019; White et al., 2020).

Spatially explicit models have been developed to represent the spatio-temporal dynamics of *Xf* outbreaks across different spatial scales and outbreak scenarios. These include reaction-diffusion equations (Aniţa et al., 2021; Gilioli et al., 2023; Martin et al., 2021), ordinary differential equation systems (Cendoya et al., 2024), and lattice-based framework (Fierro et al., 2019). Models that explicitly integrate vector population dynamics provide a more comprehensive and mechanistic representation of vector-driven transmission processes (Fierro et al., 2019; Gilioli et al., 2023; Giménez-Romero et al., 2023). Additionally, studies have explored the influence of ground cover plants on the *Xf* pathosystem, considering their potential role in disease persistence and vector ecology (Aniţa et al., 2021; Brunetti et al., 2020; Fierro et al., 2019).

These modelling frameworks have provided valuable insights into *Xf* epidemiology, and some are already employed as tools to support Pest Risk Assessment (PRA) and pest risk management. Nonetheless, there remains a need for models that can inform the design and implementation of effective management strategies under the Integrated Pest Management (IPM) framework to achieve effective and sustainable control of *Xf*-associated diseases in infected scenarios. Such models must mechanistically integrate the key physiological and bioecological processes underlying vector and bacterial population dynamics, including vector-host plant interactions, disease transmission and symptom progression, to accurately simulate *Xf* epidemiology.

Our study presents a novel physiologically-based eco-epidemiological model for *Xf* in olive agro-ecosystems. The model adopts a mechanistic framework that explicitly incorporates the influences of environmental and meteorological variables on vector phenology, mortality, and disease dynamics within the host plants, as well as the seasonality of vector-host interactions and vector preferences on transmission. The model captures population dynamics and disease progression through a compartmental model, where compartments represent both vector lifestages and host health status classes. The eco-epidemiological system is formulated as a system of ordinary and delayed differential equations, allowing for a detailed and dynamic representation of the plant-vector-bacterium interactions.

While the model is calibrated using the *Xf* outbreak in Apulia as a case study, its mechanistic representation of disease dynamics in olive agro-ecosystems is designed to be generalizable across diverse contexts and environments. The results, based on this calibration, provide novel insights into infection dynamics and demonstrate the potential of the approach for broader applications to advance understanding and management of *Xf* epidemiology. The model framework adheres to the principles of Good Modelling Practice (GMP) outlined by Jakeman et al. (2024), through detailed conceptualization and justification of modelling choices, clear acknowledgment of limitations, and application to a relevant real-world case study, while retaining flexibility for extension and application to other plant–pathogen systems and management scenarios.

2. Material and methods

A physiologically-based eco-epidemiological model was developed to simulate the dynamics of *Xf* in olive agroecosystems. The model provides a mechanistic representation of *Xf* epidemiology (Fig. 1) by integrating key bioecological processes, including vector population dynamics, vector–plant interactions, disease transmission, growth of non-olive vegetation, and disease progression in infected olive trees. It is formulated as a compartmental system of ordinary and delayed differential equations that explicitly incorporates vector life stages, host infection status, and environmental drivers.

The vector population is structured into three compartments: preimaginal stages (P), susceptible adults (V_S), and infected adults (V_I). Vegetation is structured into different groups: (i) non-host plants, composed by herbaceous vegetation (H) and non-host shrubs and trees (N); (ii) reservoir shrubs and trees, divided into susceptible (R_S) and infected (R_I) compartments; and (iii) olive trees (crops), represented by seven compartments corresponding to successive stages of disease progression ($C_S,\ C_0 - C_5$) (Table 1).

The vector population considered in this model refers to *P. spumarius*, which follows a univoltine life cycle. Briefly, preimaginal stage (P) overwinter in diapause and resume development when temperature conditions become suitable (Cornara et al., 2018). Their development rate is determined by a temperature-dependent model adapted from the *P. spumarius* phenological model developed by Gilioli et al. (2024). Adult vectors emerge non-infected in early spring and undergo ovarian parapause, delaying oviposition during periods of extended photoperiod (Witsack, 1973). Mortality of both preimaginal (P) and adult vector stages (V_S and V_I) is modelled using temperature-dependent functions, and fecundity is defined by a constant rate during the reproductive phase. Preimaginal and adult stages are constrained within $[0, K_P]$, where K_P (ha^{-1}) denotes the carrying capacity for preimaginal vectors.

Adult vectors are assumed to move and interact with all vegetation compartments for shelter and food source, with infected vegetation also serving as a source of bacterial inoculum to susceptible vectors. This movement is implicitly modelled through a vector-plant contact function dependent on vegetation abundance and vector preference for different vegetation compartments. This preference follows a seasonal pattern influenced by temperature and host plant suitability (Bodino et al., 2023), and is further affected by the disease status of olive trees, with highly symptomatic trees being less attractive to the insects (Daugherty et al., 2011). Contact between susceptible adult vectors and infectious vegetation may result in bacterial acquisition, with the effective acquisition rate depending on the level of infection assumed for the vegetation compartment. Contact between infected adult vectors and susceptible vegetation may result in bacterial transmission without a latent period (Cornara et al., 2018), with infection rate depending on the density of infected vectors in contact with susceptible vegetation and the susceptibility of the host compartment. Additionally, contact between infected vectors and already infected olive trees is assumed to generate superinfection events, which contribute to accelerating disease progression within the host.

Olive trees are represented as the number of trees per unit area, determined by the planting density of the olive grove, and constitute the crop compartment. They are classified into seven categories according to infection status and percentage of canopy desiccation: susceptible olive trees (C_S), latent trees (C_0), infectious asymptomatic trees (C_1), and symptomatic trees with $(0\%, 25\%]$ (C_2), $(25\%, 50\%]$ (C_3), $(50\%, 75\%]$ (C_4), and $(75\%, 100\%]$ (C_5) canopy desiccation (Table 1). Symptomatic classes follow the definitions of Hornero et al. (2020). The total number of olive trees remains constant throughout the simulations. Disease progression dynamics are described by functions depending on

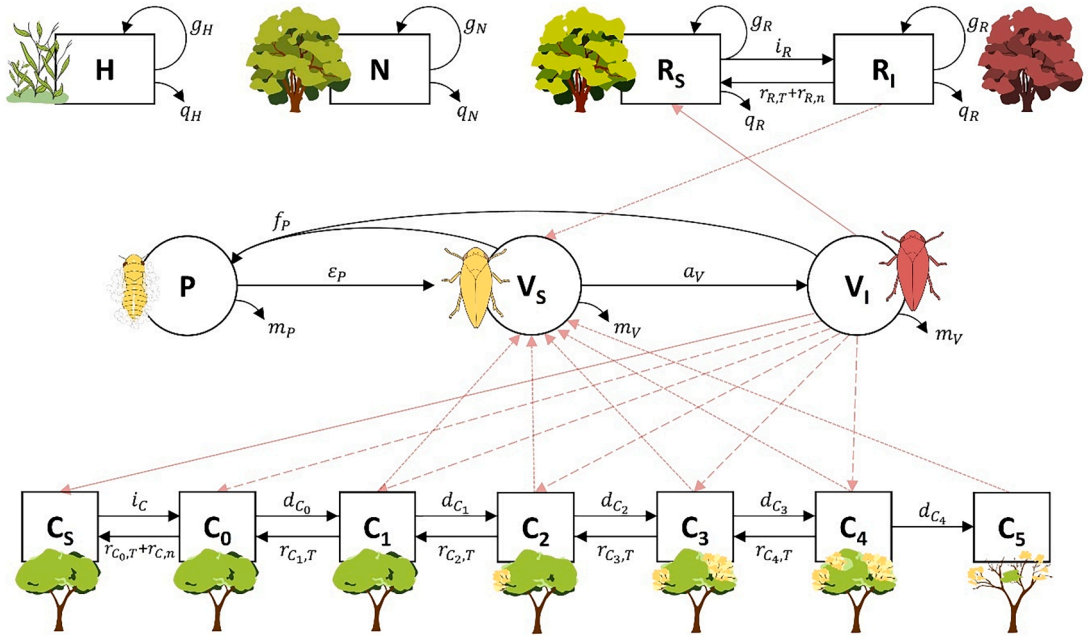

Fig. 1. Schematic representation of the eco-epidemiological model framework. Rectangles represent vegetation compartments, while circles denote vector compartments. Solid black arrows denote vegetation dynamics, demographic processes, and transitions between compartments. Red arrows depict vector–host plant interactions that determine vector acquisition (dotted arrows) from infectious plants, infection events by infected vectors (solid arrows), and superinfection events (dashed arrows) by infected vectors. Definitions of model compartments and functions are provided in Table 1.

temperature, soil water availability, and the density of infected vectors (Godefroid et al., 2019; Sicard et al., 2018; Sun et al., 2013). Extreme temperatures are assumed to reduce bacterial populations within the plant (Feil and Purcell, 2001) allowing for partial disease regression, except in advanced disease stages (i.e., C_5).

Herbaceous vegetation (H) non-host to *Xf* is assumed to uniformly cover the field and is modelled as biomass per area unit, constrained to non-negative values. Biomass varies over time and is limited by sub-optimal air temperature (T_{AD}), limited incident solar radiation (I_{AD}), and reduced proportion of soil water content (W).

Non-host shrubs and trees (N) are modelled as biomass per area unit, constrained within the range $[0,\ K_N]$, where K_N (kg ha^{-1}) represents the field's carrying capacity for the N vegetation compartment. The combined biomass of reservoir shrubs and trees is constrained within $[0,\ K_R]$, where K_R (kg ha^{-1}) is the field's carrying capacity for this compartment. The biomass of both non-host and reservoir shrubs and trees varies over time and is described by a temperature-dependent function. A proportion of these woody plants consists of deciduous species that shed their foliage in autumn.

The simulated landscape represents a one-hectare olive grove, structured into four vegetation compartments: ground cover vegetation, non-host shrubs and trees, reservoir shrubs and trees, and olive trees. Given the small spatial scale, spatial constraints are neglected, and the landscape is considered isolated with no in- or outflow of vectors, allowing only local epidemiological dynamics.

2.1. Formal model

Seven ordinary differential equations (ODEs) describe the dynamics of non-olive plants and vectors (i.e., H, N, R_S, R_I, P, V_S, and V_I). Delay differential equations (DDEs) were used to represent the progression of olive trees through consecutive disease stages. This approach incorporates minimum delay period (τ_{C_i}, with $i \in \{0, 1, \ldots, 4\}$) for the infected olive tree compartments (C_0–C_4), which reflects the slow within-host dynamics of *Xf* and the prolonged duration of asymptomatic and early symptomatic phases (Saponari et al., 2019), ensuring that trees remain in each stage at least the specified duration before progressing to the next. Fixed delays were adopted as a pragmatic compromise between biological realism, model tractability, and data availability for parameterization. The term $C_i^*(t, \tau_{C_i})$ denotes the number of olive trees at time t that have persisted in stage i for at least the corresponding delay period τ_{C_i}.

Overall, the eco-epidemiological model consists of 14 differential equations, one corresponding to each compartment. For clarity, the functions are presented bellow as a system of equations without explicit parameters definitions, except for time and delay terms:

(a) $\frac{dH}{dt}(t) = g_H(t) - q_H(t)\cdot H(t)$

(b) $\frac{dN}{dt}(t) = g_N(t)\cdot N(t) - q_N(t)\cdot N(t)$

(c) $\frac{dR_S}{dt}(t) = g_R(t)\cdot R_S(t) - q_R(t)\cdot R_S(t) + r_{R,T}(t)\cdot R_I(t) + r_{R,n}(t) - i_R(t)\cdot R_S(t)$

(d) $\frac{dR_I}{dt}(t) = g_R(t)\cdot R_I(t) + i_R(t)\cdot R_S(t) - q_H(t)\cdot R_I(t) - r_{R,T}(t)\cdot R_I(t) - r_{R,n}(t)$

(e) $\frac{dP}{dt}(t) = f_P(t)\cdot(V_S(t) + V_I(t)) - \varepsilon_P(t)\cdot P(t) - m_P(t)\cdot P(t)$

(f) $\frac{dV_S}{dt}(t) = \varepsilon_P(t)\cdot P(t) - a_V(t)\cdot V_S(t) - m_V(t)\cdot V_S(t)$

$$\text{(g)}\ \frac{dV_I}{dt}(t) = a_V(t)\cdot V_S(t) - m_V(t)\cdot V_I(t) \tag{1}$$

(h) $\frac{dC_S}{dt}(t) = r_{C_o,T}(t)\cdot C_0^*(t, \tau_{C_0}) + r_{C,n}(t) - i_C(t)\cdot C_S(t)$

(i) $\frac{dC_0}{dt}(t) = i_C(t)\cdot C_S(t) + r_{C_1,T}(t)\cdot C_1^*(t, \tau_{C_1}) - d_{C_0}(t)\cdot C_0^*(t, \tau_{C_0}) - r_{C_o,T}(t)\cdot C_0^*(t, \tau_{C_0}) - r_{C,n}(t)$

(j) $\frac{dC_1}{dt}(t) = d_{C_0}(t)\cdot C_0^*(t, \tau_{C_0}) + r_{C_2,T}(t)\cdot C_2^*(t, \tau_{C_2}) - d_{C_1}(t)\cdot C_1^*(t, \tau_{C_1}) - r_{C_1,T}(t)\cdot C_1^*(t, \tau_{C_1})$

(k) $\frac{dC_2}{dt}(t) = d_{C_1}(t)\cdot C_1^*(t, \tau_{C_1}) + r_{C_3,T}(t)\cdot C_3^*(t, \tau_{C_3}) - d_{C_2}(t)\cdot C_2^*(t, \tau_{C_2}) - r_{C_2,T}(t)\cdot C_2^*(t, \tau_{C_2})$

(l) $\frac{dC_3}{dt}(t) = d_{C_2}(t)\cdot C_2^*(t, \tau_{C_2}) + r_{C_4,T}(t)\cdot C_4^*(t, \tau_{C_4}) - d_{C_3}(t)\cdot C_3^*(t, \tau_{C_3}) - r_{C_3,T}(t)\cdot C_3^*(t, \tau_{C_3})$

(m) $\frac{dC_4}{dt}(t) = d_{C_3}(t)\cdot C_3^*(t, \tau_{C_3}) - d_{C_4}(t)\cdot C_4^*(t, \tau_{C_4}) - r_{C_4,T}(t)\cdot C_4^*(t, \tau_{C_4})$

Table 1
Summary of model state variables and functions of the overall Eco-epidemiological model.

Symbol	Description	Units
	State variables	
H	Herbaceous vegetation	kg ha^{-1}
N	Non-host shrubs and trees	kg ha^{-1}
R_S	Susceptible reservoirs	kg ha^{-1}
R_I	Infected reservoirs	kg ha^{-1}
P	Preimaginal vector stage	insects ha^{-1}
V_S	Susceptible adults	insects ha^{-1}
V_I	Infected adults	insects ha^{-1}
C_S	Susceptible olive trees	plants ha^{-1}
C_0	Latent olive trees	plants ha^{-1}
C_1	Infectious asymptomatic olive trees	plants ha^{-1}
C_2	Initial severity, with >0 to 25 % canopy with desiccated branches	plants ha^{-1}
C_3	Medium severity, with >25 to 50 % canopy with desiccated branches	plants ha^{-1}
C_4	High severity, with >50 to 75 % canopy with desiccated branches	plants ha^{-1}
C_5	Very high severity, with >75 % canopy with desiccated branches or fully desiccated trees	plants ha^{-1}
C_i^*	Number of olive trees that have persisted in infection stage i (with $i \in \{0,1,\ldots,4\}$) for at least the corresponding delay period	plants ha^{-1}
	Functions or parameters	
Herbaceous vegetation		
g_H	Growth function of herbaceous vegetation	
q_H	Senescence function of herbaceous vegetation	
Non-host shrubs and trees		
g_N	Growth rate function of non-host shrubs and trees	
q_N	Senescence function of the deciduous biomass of non-host shrubs and trees	
Reservoir shrubs and trees		
g_R	Growth rate function of infected and susceptible reservoir shrubs and trees	
q_R	Senescence rate function of the deciduous reservoir biomass during autumn	
i_R	Infection rate function of susceptible reservoir shrubs and trees by infected vectors	
$r_{R,T}$	Temperature-dependent disease recovery rate function of infected reservoir shrubs and trees due to low winter temperatures	
$r_{R,n}$	Non-systemic infection recovery rate function of infected reservoir shrubs and trees	
Insect vectors		
f_P	Fecundity rate function of adult vectors	
ε_P	Emergence rate function of adult vectors	
m_P	Mortality rate function of preimaginal vectors	
m_V	Mortality rate function of adult vectors	
a_V	Acquisition rate function of susceptible vectors from infectious vegetation compartments	
Crop - Olive trees		
i_C	Infection rate function of susceptible olive trees by infected vectors	
d_{C_i}	Disease progression rate function describing the transition rate of olive trees from disease stage i to the next disease stage	
$r_{C_i,T}$	Temperature-dependent disease regression rate function of infected olive trees of disease stage i	
$r_{C,n}$	Non-systemic infection recovery rate function of infected olive trees of disease stage C_0	

(n) $\frac{dC_5}{dt}(t) = d_{C_4}(t) \cdot C_4^*(t, \tau_{C_4})$

The state variables presented in Eq. (1) are summarised in Table 1. A detailed description of the model's functions and parameters associated with vector population dynamics is provided in Section 2.2, while the functions describing vector–host contact, bacterial transmission, and disease progression are presented in Section 2.3. The biomass dynamics of non-olive vegetation compartments are described in Section 2.4.

The ODE-DDE system (Eq. (1)) is solved numerically in MATLAB (version R2024a) by the explicit second-order Runge-Kutta method (Quarteroni et al., 2014) with a constant time-step of one hour. Being the time-step constant, no interpolation is required to evaluate the delayed state variables. To compute the state variables at the new time-step t_{n+1}, the ODEs are treated in a standard way by exploiting all the state variables involved in the equation at time t_n, while each DDE is integrated by using the corresponding state variable at the time-step $t_{n-\tau}$ (where τ is the delay associated with the state variable) and the other state variables at time t_n.

2.2. Vector population dynamics (P, V_S and V_I)

The vector population dynamic defined in Eqs. (1e)–(1 g) is governed by the fecundity function ($f_P(D_{OY}, L_{DD})$, the emergence function ($\varepsilon_P(t, T_{AH})$), the mortality function of preimaginal ($m_P(D_{OY}, T_{AH}, P)$) and adult stages ($m_V(D_{OY}, T_{AH})$), and acquisition function ($a_V(R_I, C_1, C_2, C_3, C_4)$, see Section 2.3).

2.2.1. Fecundity function (f_P)

We assumed a constant oviposition rate function during the reproductive phase of vector females, described as:

$$f_P(D_{OY}, L_{DD}) = \begin{cases} f_{P,or} \cdot f_{P,sr} & \text{if } D_{P,\min}(L_{DD}) \le D_{OY} \le D_{P,\max} \\ 0 & \text{otherwise} \end{cases} \quad (2)$$

where:

- $f_{P,or}$: oviposition rate per female vector (h^{-1}), defined based on reports on the average fecundity recorded (Di Serio et al., 2019; Silva et al., 2015), and to maintain a stable vector population over the years of simulation,
- $f_{P,sr}$: average sex ratio of *P. spumarius* population during the oviposition period, estimated based on Bodino et al. (2023), representing a higher proportion of females during this period,
- $D_{P,min}(L_{DD})$: onset of oviposition period corresponding to the day of the year (D_{OY}) when daylight duration (L_{DD}) drops below a critical threshold ($L_{P,f}$) towards late summer (Avosani et al., 2021; Morente et al., 2021; Witsack, 1973),
- $D_{P,max}$: end of the oviposition period and maximum adult longevity after which adult populations are rarely observed in the field, set at November 15 considering Apulian conditions (Bodino et al., 2023).

Parameter values for Eq. (2) are reported in Table S1 (Section S1) of Supplementary Material.

2.2.2. Emergence function (ε_P)

The emergence function of the preimaginal stage ($\varepsilon_P(t, T_{AH})$) is determined by a satellite model adapted from the *P. spumarius* phenological model developed by Gilioli et al. (2024). This stage-structured population model is formulated as a system of Kolmogorov PDEs that accounts for both chronological time and the physiological age of insect stages. The relative cumulative emergence curve generated by this phenological model is integrated into the eco-epidemiological framework through the emergence function $\varepsilon_P(t, T_{AH})$ defined as:

$$\varepsilon_P(t, T_{AH}) = \text{Kolmogorov}(t, T_{AH}) \quad (3)$$

where Kolmogorov represents the PDE system defining the phenological model in Gilioli et al. (2024) as function of the average hourly temperature ($T_{AH}(t)$). The simulation of the phenological model begins on January 1, when preimaginal individuals are assumed to be in diapause. Diapause termination is determined by the accumulation of degree-days by preimaginal stage according to Gilioli et al. (2024). Development rate

$z_P(T_{AH})$ (h^{-1}) of post-diapausing preimaginal stage is determined by the temperature-based Brière equation:

$$z_P(T_{AH}) = \begin{cases} z_{P,a} \cdot T_{AH} \cdot \left(T_{AH}(t) - T_{P,z\ inf}\right) \cdot \sqrt{T_{P,z\ sup} - T_{AH}(t)} & \text{if } T_{P,z\ inf} \le T_{AH}(t) \le T_{P,z\ sup} \\ 0 & \text{otherwise} \end{cases} \quad (4)$$

where $z_{P,a}$ is an empirical constant (dimensionless), $T_{P,z\ inf}$ and $T_{P,z\ sup}$ are the lower and the upper development temperature thresholds (°C), defined according to the optimization procedure reported by Gilioli et al. (2024). The parameter estimates for Eq. (4) are reported in Table S1.

2.2.3. Preimaginal mortality function (m_P)

The mortality function of preimaginal stage ($m_P(D_{OY}, T_{AH}, P)$) combines intrinsic temperature-dependent mortality (abiotic) with extrinsic mortality related to natural control factors. The function is defined as:

$$m_P(D_{OY}, T_{AH}, P) = \begin{cases} m_{P,T}(T_{AH}) \cdot \left[1 + \left(\frac{P(t)}{K_P}\right)^2\right] & \text{if } D_{OY} \ge D_{P,m}(T_{AH}) \\ 0 & \text{otherwhise} \end{cases} \quad (5)$$

where $m_{P,T}(T_{AH})$ represents the temperature-dependent mortality function, incorporating both abiotic and extrinsic factors. This term is modulated by a density-dependent mortality component linked to the maximum insect abundance sustained in the landscape (K_P) based on Yurtsever (2000). Preimaginal mortality is considered only after diapause termination (see Section 2.2.2). Accordingly, preimaginal mortality is neglected from oviposition in the previous year until diapause termination of following year.

Temperature-dependent mortality is modelled using a function adapted from Gilioli et al. (2016), and is expressed as:

$$m_{P,T}(T_{AH}) = \begin{cases} m_{P,n} \cdot \left[\left(T_{P,z\,inf} - T_{AH}(t)\right)^2 + 1\right] & \text{if } T_{AH}(t) < T_{P,z\,inf} \\ -z_P(T_{AH}) \cdot \ln\left[1 - \mu_{P,T}(T_{AH})\right] + m_{P,n} & \text{if } T_{P,z\,inf} \le T_{AH}(t) \le T_{P,z\,sup} \\ m_{P,n} \cdot \left[\left(T_{AH}(t) - T_{P,z\,sup}\right)^2 + 1\right] & \text{if } T_{AH}(t) > T_{P,z\,sup} \end{cases} \quad (6)$$

where:

- $m_{P,n}$: extrinsic mortality due to natural control factors (h^{-1}), defined based on field monitoring data of *P. spumarius* collected in 10 olive groves in the Apulian region in 2019 (C. Dongiovanni, unpublished data),
- $z_P(T_{AH})$: development rate function (Eq. (4)),
- $T_{P,z\ inf}$, and $T_{P,z\ sup}$ are the minimum and maximum development temperature thresholds (°C), respectively,
- $\mu_{P,T}(T_{AH})$: average stage proportional mortality of *P* defined as:

$$\mu_{P,T}(T_{AH}) = \begin{cases} 0.75 \cdot \left(\frac{T_{P,z\ inf}}{T_{P,\ \mu\ opt}} - 1\right)^{-2} \cdot \left(\frac{T_{AH}(t) - T_{P,\ \mu\ opt}}{T_{P,\ \mu\ opt}}\right)^2 + 0.1 & \text{if } T_{P,z\ inf} \le T_{AH}(t) \le T_{P,z\ sup} \\ 0.85 & \text{otherwise} \end{cases} \quad (7)$$

where $T_{P,\ \mu\ opt} = \frac{T_{P,z\ inf} + T_{P,z\ sup}}{2}$.

Parameters values for Eqs. (5)–(7) are reported in Table S1.

2.2.4. Adult mortality function (m_V)

The mortality of adult stage ($m_V(D_{OY}, T_{AH})$) is defined by combination of ageing process and temperature-dependent mortality:

$$m_V(D_{OY}, T_{AH}) = 1 - \left[1 - m_{V,T}(T_{AH})\right] \cdot \left[1 - m_{V,a}\right] \quad (8)$$

where $m_{V,a}$ describes the mortality rate due to ageing process (h^{-1}), assuming an average adult longevity in Apulian conditions of 170 days (Bodino et al., 2023), and $m_{V,T}(T_{AH})$ denotes a temperature-dependent mortality function that incorporates extrinsic mortality related to natural control factors (h^{-1}). The function $m_{V,T}(T_{AH})$ is defined as:

$$m_{V,T}(T_{AH}) = \begin{cases} m_{V,n} \cdot \left[\left(T_{V,m\ inf} - T_{AH}(t)\right)^2 + 1\right] & \text{if } T_{AH}(t) < T_{V,m\ inf} \\ m_{V,Ta} \cdot \left(m_{V,Tb}\right)^{T_{AH}(t)} + m_{V,n} & \text{if } T_{AH}(t) \ge T_{V,m\ inf} \end{cases} \quad (9)$$

where:

- $m_{V,n}$: extrinsic mortality due to natural control factors (h^{-1}),
- $T_{V,m\ inf}$: lower temperature threshold (°C) in which mortality formula changes,
- $m_{V,Ta}$, $m_{V,Tb}$: dimensionless parameters shaping the temperature-dependent mortality.

The functional form and the parameters of Eq. (9) were defined based on laboratory experimental data on the effect of temperature on *P. spumarius* adult mortality were used to estimate the temperature-dependent mortality rate function (J.A. Navas-Cortés, unpublished data). Parameter estimates for Eqs. (8) and (9) are reported in Table S1.

2.3. Epidemiological functions

2.3.1. Vector-plant contact function (n_j)

Adult movement among vegetation compartments drives the acquisition (a_V) and infection (i_C, i_R) processes through the contact between vector and host plant. It is modelled through a vector-plant contact function ($n_j(J)$) described by a modified Monod functional response, which depends on vegetation abundance ($J(t)$) and vector preference $\left(p_j\right)$ for different vegetation compartments (j). This formulation provides a biologically realistic representation of how contact rates respond to changes in host abundance, capturing the limited capacity of adult vectors to exploit host plants. The vector-plant contact function is defined as:

$$n_j(J) = \frac{p_j \cdot J(t)}{\lambda_j + J(t)} \tag{10}$$

where λ_j is the j-th semi-saturation constant of the functional response (with the same unit as the corresponding vegetation compartment; see Table S3, Supplementary Material). To obtain the proportion of vectors feeding on a given vegetation compartment per time unit ($\widehat{n}_j(J)$), the Eq. (10) is normalized as:

$$\widehat{n}_j(J) = \frac{n_j(J)}{\sum_{j'} n_{j'}(J')} \tag{11}$$

The seasonal dynamics of *P. spumarius* among the vegetation compartments over the year observed in Apulian agroecosystems were described using preference values that varied across two distinct periods of the year (Bodino et al., 2023; Cavalieri et al., 2019; Cornara et al., 2018): (i) higher preferences for olive trees (C_S–C_4) and for non-cultivated shrubs and trees (corresponding to vegetation compartments N, R_S and R_I), in the warm season (early June to late September in Apulia), (ii) higher preference for herbaceous vegetation (H) during the rest of the year. Monitoring data of *P. spumarius* adults in Apulian fields during 2019 (C. Dongiovanni, unpublished data) were used to estimate the vector preferences for each vegetation compartment and the transition between the two preference periods, determined by thermal and chilling requirements. Detailed description of parameter estimates is described in the Section S1.1 of Supplementary Material.

2.3.2. *Acquisition function* (a_V)

Vector acquisition is assumed to depend on the bacterium titre within the infected plant and the feeding activity by the vector (Gilioli et al., 2023). Assuming that each vector feeds on one host plant per time unit, the acquisition rate is defined as:

$$\begin{aligned} a_V(R_I, C_1, C_2, C_3, C_4) = {} & a_{R_I} \cdot \widehat{n}_{R_I}(R_I) + a_{C_1} \cdot \widehat{n}_{C_1}(C_1) + a_{C_2} \cdot \widehat{n}_{C_2}(C_2) \\ & + a_{C_3} \cdot \widehat{n}_{C_3}(C_3) + a_{C_4} \cdot \widehat{n}_{C_4}(C_4) \end{aligned} \tag{12}$$

where the acquisition rate corresponds to the proportion of insects feeding on infectious vegetation (given by $\widehat{n}_j(J)$, Eq. (11)) per time unit, weighted by the probability of acquiring the bacterium from the respective vegetation compartment (a_j, h^{-1}).

The bacterium titres for each olive stage were assigned based on literature data (De Pascali et al., 2022; Hill and Purcell, 1997; Saponari et al., 2017, 2019) and are presented in Table S2 (Section S1.2) of Supplementary Material. For latent olive trees (C_0), the same bacterium threshold level for effective acquisition observed in grapevines by Hill and Purcell (1997) was assumed. Considering a maximum acquisition rate at 0.1206 (EFSA PLH Panel, 2019), the acquisition probabilities (a_j) were estimated from literature (Bodino et al., 2021; Cavalieri et al., 2019; Cornara et al., 2017). The acquisition rate from infected reservoir shrubs and trees (a_{R_I}) was assumed the same rate as for mild symptomatic olive trees (C_2) (see Table S2).

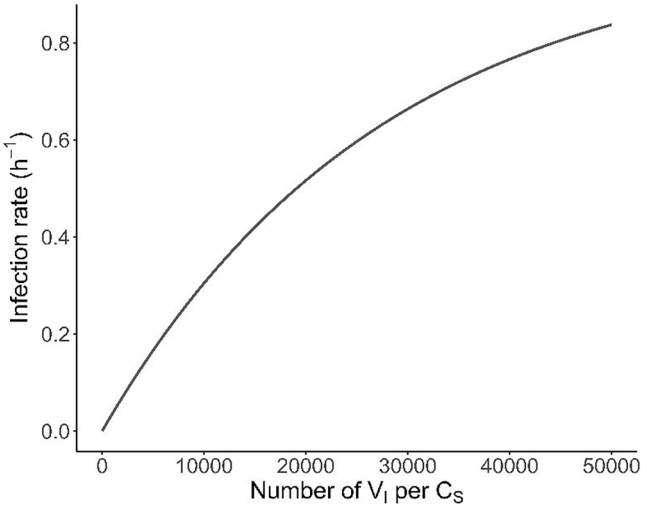

Fig. 2. Representation of the infection function $i_C(C_S, V_I)$ (Eq. (5)), illustrating the rate of infection of susceptible olive tree (C_S) as function of the density of infected vectors (V_I).

2.3.3. *Infection function* (i_C *and* i_R)

Susceptible olive trees (C_S) and reservoirs (R_S) may become infected through contact with infected vectors (V_I). The probability of infection depends on the number of V_I feeding on a susceptible tree and follows a nonlinear pattern derived from the Poisson infection probability model described by Daugherty and Almeida (2009). The infection function of olive trees ($i_C(C_S, V_I)$; Fig. 2) is defined as:

$$i_C(C_S, V_I) = 1 - e^{-i_{C,sp} \cdot i_{C,ip} \cdot \left(\frac{\widehat{n}_{C_S}(C_S) \cdot V_I(t)}{C_S(t)} \right)} \tag{13}$$

where:

- $i_{C,sp}$: index of susceptibility of olive trees to *Xf* (it is a real value in [0,1]), estimated through model calibration (Section 2.6),
- $i_{C,ip}$: vector inoculation rate ($insect^{-1} \bullet h^{-1}$, in [0,1]), it is equivalent to the probability of an infected vector transmitting the bacterium to the host plants. It was estimated based on experimental data of the proportion of olive plants infected after seven days of inoculation access period by different numbers of infected *P. spumarius*, reported by Cornara et al. (2017) (see Table S1),
- $\widehat{n}_{C_S}(C_S)$: fraction of V_I feeding on C_S (in [0,1]), defined in Eq. (11).

The infection rate function of susceptible reservoir ($i_R(R_S, V_I)$) is defined by the same functional form of Eq. (13), where the parameters $i_{R,sp}$ and $i_{R,ip}$ are assumed equal to the parameters $i_{C,sp}$ and $i_{C,ip}$ of olive trees, respectively.

2.3.4. *Delay periods of infected olive tree compartments* (τ_{C_i})

The olive tree compartments are represented by a system of DDEs (Eqs. (1h)–(1n)), where the disease progression and regression functions act on the number of olive trees that have remained in the disease stage i (with $i \in \{0, 1, \ldots, 4\}$) for at least corresponding delay period τ_{C_i}, indicated by $C_i^*(t, \tau_{C_i})$. The delay periods were defined based on evidence from experimental studies (EFSA PLH Panel, 2019; Saponari et al., 2017), quantitative estimates (White et al., 2020), and complementary expert knowledge (see Table S1).

2.3.5. *Disease progression function in olive tree compartments* (d_{C_i})

The disease progression function of infected olive trees is modelled through an implicit representation of the bacterium growth and spread within the plant, as well as the resulting symptom development in olive canopy. Disease progression is influenced by temperature (affecting bacterial replication), soil water availability (reflecting the impact of water stress on symptom severity), and the density of infected vectors (capturing the effect of superinfection events on disease dynamics) (Godefroid et al., 2019; Sicard et al., 2018; Sun et al., 2013). Extreme temperatures can reduce bacterial populations within the plant, limiting the progression of the disease. The disease progression is defined as:

$$\begin{aligned} d_{C_i}(D_{OY}, T_{AH}, AW, C_i, V_I) = \max\{ & b_{C_i,TS}(D_{OY}, T_{AH}, C_i, V_I) \cdot w_{C_i}(AW) \\ & - b_{C_i,m}(T_{AH}), 0 \} \end{aligned} \tag{14}$$

where:

- $b_{C_i,TS}(D_{OY}, T_{AH}, C_i, V_I)$: disease progression rate due to cumulated bacterium growth (h^{-1}) defined as function of the day of the year

(D_{OY}), average hourly temperature (T_{AH}, °C), and on the populations C_i and V_I,
- $w_{C_i}(AW)$: disease progression factor due to water stress (dimensionless) as function of soil available water (AW, mm),
- $b_{C_i,m}(T_{AH})$: disease regression rate (h^{-1}) due to bacterium mortality by adverse temperature (T_{AH}).

The disease progression rate due to cumulated bacterium growth ($b_{C_i,TS}(D_{OY}, T_{AH}, C_i, V_I)$) is defined as:

$$b_{C_i,TS}(D_{OY}, T_{AH}, C_i, V_I) = \begin{cases} b_{C_i,TS\ sp} \cdot b_{C_i,T}(D_{OY}, T_{AH}) \cdot \left[1 + b_{C_i,S}(C_i, V_I)\right] & \text{if } D_{C,sp}(T_{AH}) \le D_{OY} \le D_{C,dp}(T_{AH}) \\ 0 & \text{otherwise} \end{cases} \quad (15)$$

where $b_{C_i,TS\ sp}$ is the stage-specific shape parameter estimated from experimental data from Saponari et al. (2017). The temperature-dependent growth function ($b_{C_i,T}(D_{OY}, T_{AH})$) defines the cumulated bacterium growth rate during the delay period (τ_{C_i}) for each disease stage (C_i), and was modelled using the function adapted from Analytis (1977):

$$b_{C_i,T}(D_{OY}, T_{AH}) = \int_{t-\tau_{C_i}}^{t} b_{C,T1} \cdot \left(T_{AH}(s) - T_{C,inf}\right)^{b_{C,T2}} \cdot \left(T_{C,sup} - T_{AH}(s)\right)^{b_{C,T3}} \cdot \chi(D_{OY}, T_{AH}) ds \quad (16)$$

where:

- $b_{C,T1}$, $b_{C,T2}$ and $b_{C,T2}$: empirical constants (dimensionless),
- $T_{C,inf}$ and $T_{C,sup}$: lower and upper temperature thresholds for bacterial growth (°C),
- $\chi(D_{OY}, T_{AH})$: defines the range of temperature and time of the function:

$$\chi(D_{OY}, T_{AH}) = \begin{cases} 1 & \text{if } T_{C,inf} \le T_{AH}(t) \le T_{C,sup} \text{ and } D_{C,sp}(T_{AH}) \le D_{OY} \le D_{C,dp}(T_{AH}) \\ 0 & \text{otherwise} \end{cases}$$

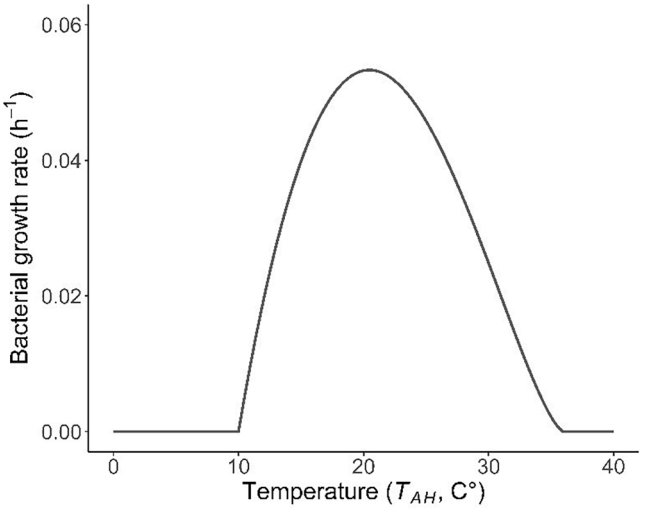

Fig. 3. Representation of the temperature-dependent bacterial growth function $b_{C_i,T}(D_{OY}, T_{AH})$ for *Xylella fastidiosa* subsp. *pauca* (Eq. (16)).

Parameters of the Eq. (16) were estimated based on in vitro experimental data evaluating the growth of *Xf* subsp. *pauca* under different temperatures (J.A. Navas-Cortés, unpublished data; Fig. 3).

Bacterium growth and disease progression is assumed to occur between the onset of the olive tree sprouting in spring ($D_{C,sp}(T_{AH})$) and the onset of dormancy in late autumn ($D_{C,dp}(T_{AH})$), while growth is arrested during dormancy period of olive trees due to unsuitable climatic conditions and low host plant physiological activity (Saponari et al., 2017). The sprouting phase in olive trees is defined by a chilling and forcing model adapted from Didevarasl et al. (2023). The onset of dormancy phase is defined by the accumulation of chilling hours according to the model proposed by López-Bernal et al. (2020).

The cumulative bacterium growth in infected olive trees can be accelerated by superinfection events ($b_{C_i,S}(C_i, V_I)$), which occurs when infected vectors (V_I) transmit *Xf* to the infected olive trees (C_i) during the delay period. The contribution is defined as:

$$b_{C_i,S}(C_i, V_I) = b_{C_i,Sp} \cdot \min\left\{ \frac{1}{b_{C_i,S\ max}} \cdot \int_{t-\tau_{C_i}}^{t} \frac{\widehat{n}_{C_i}(C_i) \cdot V_I(s)}{C_i(s)} ds, 1 \right\} \quad (17)$$

where $b_{C_i,Sp}$ (dimensionless) is a constant representing the maximum rate at which superinfection contributes to cumulative bacterium growth within an infected olive tree. This effect is modulated by the cumulative number of superinfection events experienced by a tree in stage C_i during the delay period, normalized by the maximum number of superinfection events $b_{C_i,S\ max}$ (vector · plant^{-1}), which is assumed under high vector density based on Di Serio et al. (2019). Parameter values of $b_{C_i,Sp}$ were defined based on conservative assumptions reflecting the current limited empirical knowledge of this process. Specifically, lower values were assigned to advanced disease stages, assuming that superinfection in heavily infected olive trees has a lower relative impact on the bacterium population within the plant.

The disease progression rate is modulated by water stress function $w_{C_i}(AW)$ adapted from the water stress coefficient defined by Allen et al. (1998), and is determined by the accumulation of water stress during a period τ_w, set to 30 days (720 h), normalized by the maximum water stress during the same period. The function assumes that trees under low water stress conditions (i.e., low $w_{C_i}(AW)$ values, where $w_{C_i}(AW) \in [0, 1]$) exhibit a slower progression of disease symptoms, and that advanced disease stages are more susceptible to water stress (De Pascali et al., 2022). The function is defined as:

$$w_{C_i}(AW) = 1 - \frac{1}{\tau_w} \cdot \int_{t-\tau_w}^{t} \min\left\{ w_{C_i,k} \cdot \frac{AW(t)}{AWC - RAW}, 1 \right\} ds \quad (18)$$

where:

- $AW(t)$: soil available water (mm) (Allen et al., 1998),
- AWC: soil available water capacity at field capacity (mm) for olive trees, defined based on Castellini et al. (2020),
- RAW: readily available water (mm), defined based on the reference water stress coefficient for olive trees defined by FAO (Allen et al., 1998),
- $w_{C_i,k}$: parameter (dimensionless) describing the effect of *Xf* infection on olive tree susceptibility to water stress, estimated based on

experimental data from De Pascali et al. (2022). The progression from C_0 to C_1 stages, both asymptomatic stages, was assumed independent of water stress.

The bacterial mortality rate ($b_{C_i,m}(T_{AH})$), adapted from Giménez-Romero et al. (2022), is described by a temperature-dependent function that integrates the combined effects of cold and heat stress on bacterial survival. It is defined as:

$$b_{C_i,m}(T_{AH}) = 1 - \frac{b_{C_i,m\ sp}}{b_{C_i,m\ sp} + (TF(T_{AH}))^3} \tag{19}$$

where $b_{C_i,m\ sp}$ is a shape parameter (dimensionless) specific for the disease stage C_i, and $TF(T_{AH})$ represents the temperature factor accounting for the effects of cold and hot temperatures on bacterial mortality. $TF(T_{AH})$ is defined as:

$$TF(T_{AH}) = \frac{1}{24}\cdot\int_{t-\tau_{C_i}}^{t} y(s)ds,\ \text{with } y(s)$$
$$= \begin{cases} T_{C,cold} - T_{AH}(s) & \text{if } T_{AH}(s) < T_{C,cold} \\ 15.4\cdot(T_{AH}(s) - T_{C,hot}) & \text{if } T_{AH}(s) > T_{C,hot} \\ 0 & \text{otherwise} \end{cases} \tag{20}$$

where $T_{C,cold}$ is the lower temperature threshold for cold stress accumulation, defined based on Lieth et al. (2011), $T_{C,hot}$ is the upper threshold for heat stress, and 15.4 is a conversion parameter estimated based on in vitro experimental data (J.A. Navas-Cortés, unpublished data). The parameterization of $b_{C_i,m}(TF)$ was performed under the assumption that the accumulation of cold temperatures ($TF(T_{AH})$) during cold season in the northernmost commercial olive-growing regions in Europe (i.e., provinces of Sondrio and Trento in northern Italy; Gambella et al., 2021) is likely to induce high rates of disease regression, based on the climatic suitability patterns estimated by species distribution models (EFSA PLH Panel, 2019; Godefroid et al., 2019). Parameters values for Eqs. (15)–(20) are reported in Table S1.

2.3.6. Temperature-dependent disease regression function in olive tree compartment ($r_{C_i,T}$)

Infected olive trees can regress to the previous olive tree compartment due to the negative effects of cold and hot temperatures on the bacterial population within plants during the delay period. The disease regression rate function due to temperature ($r_{C_i,T}(D_{OY},T_{AH},AW,C_i,V_I)$) is defined based on Eq. (14) as:

$$r_{C_i,T}(D_{OY},T_{AH},AW,C_i,V_I) = \left|\min\left\{b_{C_i,TS}(D_{OY},T_{AH},C_i,V_I)\cdot w_{C_i}(AW) - b_{C_i,m}(T_{AH}),0\right\}\right| \tag{21}$$

which assumes that disease regression occurs when the negative effect of extreme temperatures to the bacterial survival surpasses the effect of cumulated bacterial growth and water stress in promoting the progression of the disease.

2.3.7. Temperature-dependent disease recovery function of reservoirs ($r_{R,T}$)

Infected reservoir biomass can recover from infection due to the negative effects of cold temperatures on the bacterial population within plants during winter. The recovery rate $r_{R,T}(D_{OY},T_{AH})$ is defined as (Giménez-Romero et al., 2022):

$$r_{R,T}(D_{OY},T_{AH}) = \begin{cases} 1 - \dfrac{r_{R,sp}}{r_{R,sp} + \left(CDD(T_{AH})^3\right)} & \text{if } D_{OY} = \text{April 1} \\ 0 & \text{otherwise} \end{cases} \tag{22}$$

where $r_{R,sp}$ is a dimensionless shape parameter, assumed equal to $b_{C_2,m\ sp}$ (Eq. (19)) of olive trees in stage C_2 to consider a recovery response comparable to that of olives at an intermediary disease stage. $CDD(T_{AH})$ represents the cumulative cold degree-days, calculated as the sum of hourly temperatures below the threshold $T_{R,cold}$. Cumulative cold degree-days are calculated from November 1 of the year preceding the simulation until March 31 of the simulation year. For modelling purposes, recovery is assumed to occur instantaneously at the end of winter, on April 1. Parameters values for Eq. (22) are reported in Table S1.

2.3.8. Non-systemic infection recovery function ($r_{C,n}$ and $r_{R,n}$)

In addition to the temperature-driven regression function, newly infected olive trees can recover due to the unsuccessful establishment of bacterium infection within the xylem following new inoculations ($r_{C,n}(C_S,C_0,V_I)$). This process is described by:

$$r_{C,n}(C_S,C_0,V_I) = \min\left\{r_{C,np}\cdot C_0(t), i_C(C_S,V_I)\cdot C_S(t)\right\} \tag{23}$$

The non-systemic infection recovery parameter ($r_{C,np}$) was defined through model calibration (Section 2.6), with the constraint that the number of recovered plants cannot exceed the number of new infected plants occurring during the same time unit.

The non-systemic infection recovery function of susceptible reservoir ($r_{R,n}(R_S,R_I,V_I)$) is defined by the same functional form of Eq. (23), where the parameter $r_{R,np}$ is assumed equal to the parameter $r_{C,np}$ of olive trees.

2.4. Biomass dynamics of non-olive vegetation compartments (H, N, R_S and R_I)

2.4.1. Herbaceous vegetation (H)

Herbaceous vegetation dynamics defined in Eq. (1a) are governed by a growth function ($g_H(T_{AD},I_{AD},P_{DA},PET,W,H)$) and a senescence function ($q_H(T_{AD})$).

Growth follows the model of McCall and Bishop-Hurley (2003), refined by Romera et al. (2009), selected for its simplicity and effectiveness in simulating herbage production under diverse environmental conditions. The growth function $g_H(T_{AD},I_{AD},P_{DA},PET,W,H)$ is defined as:

$$g_H(T_{AD},I_{AD},P_{DA},PET,W,H) = \alpha(I_{AD})\cdot I_{AD}\cdot g_{H,T}(T_{AD})\cdot g_{H,W}(P_{DA},PET,W)\cdot g_{H,l}(H)\cdot 10 \tag{24}$$

where:

- $T_{AD}(t)$: average daily temperature (°C),
- $I_{AD}(t)$: incident solar radiation (MJ m^{-2} day^{-1}),
- $P_{DA}(t)$: daily precipitation (mm day^{-1}),
- $PET(t)$: potential evapotranspiration (mm day^{-1}),
- $W(t)$: proportion of soil water content (dimensionless),
- $H(t)$: biomass of herbaceous vegetation (kg ha^{-1}).
- $\alpha(I_{AD})$: net photosynthesis efficiency function (g DM MJ^{-1}),
- $g_{H,T}(T_{AD})$: temperature growth factor,
- $g_{H,W}(P_{DA},PET,W)$: soil water factor,
- $g_{H,l}(H)$: efficiency of green canopy light interception factor.

A detailed description of the model structure and parameter values is provided by Romera et al. (2009).

The senescence rate of herbaceous vegetation is described by the temperature-dependent function $q_H(T_{AD})$ based on Romera et al. (2009), which accounts for the leaf lifespan (*LLS*, °C) expressed in degree days and a remobilization coefficient (*rem*) that represents the proportion of leaf content reabsorbed during senescence:

$$q_H(T_{AD}) = \max\left\{\frac{T_{AD}(t)}{LLS}\cdot(1-rem),0\right\}. \tag{25}$$

2.4.2. Non-host shrubs and trees (N)

The dynamics of non-susceptible shrubs and trees defined in Eq. (1b) are governed by a logistic growth function ($g_N(D_{OY},T_{AH},L_{DD},N)$) and a

senescence function ($q_N(L_{DD})$).

Biomass growth is assumed to occur from spring to autumn, coinciding with the period of active vegetative growth and reproductive tissue development. The growth rate function ($g_N(D_{OY}, T_{AH}, L_{DD}, N)$) is defined as:

$$g_N(D_{OY}, T_{AH}, L_{DD}, N) = g_{N,T}(D_{OY}, T_{AH}, L_{DD}) \cdot \left(1 - \frac{N(t)}{K_N}\right), \quad (26)$$

where, K_N is the field's carrying capacity for the vegetation compartment (kg ha^{-1}), and $g_{N,T}(D_{OY}, T_{AH}, L_{DD})$ is the temperature-dependent growth term adapted from Yan et al. (1996):

$$g_{N,T}(D_{OY}, T_{AH}, L_{DD}) = \begin{cases} \max\left\{g_{N,\max} - g_{N,sp} \cdot \left(T_{AH}(t) - T_{N,g\ opt}\right)^2, 0\right\} & \text{if } D_{N,\min}(T_{AH}) \le D_{OY} \le D_{N,\max}(L_{DD}, H) \\ 0 & \text{otherwise} \end{cases} \quad (27)$$

Parameters are set as follows:

- $g_{N,max}$: growth rate at optimal temperature, defined based on Pasalodos-Tato et al. (2015),
- $g_{N,sp}$: shape parameter (dimensionless, analytically defined)
- $T_{N,g\ opt}$: optimal growth temperature for woody plants (Rossi et al., 2007; Dombrowski et al., 2022).

The parameters $D_{N,min}(T_{AH})$ and $D_{N,max}(L_{DD}, H)$ define the start and end of the active vegetative growth period, corresponding to bug break at spring and the onset of foliage senescence at autumn, respectively. Bud break is assumed to occur simultaneously with olive trees (Section 2.3.5). Autumnal senescence was defined based on Jeong and Medvigy (2014) and Liu et al. (2020).

At the onset of autumnal senescence, biomass growth stops, and the deciduous fraction of the vegetation begins to lose foliage. Senescence is described as (adapted from Dufrêne et al., 2005):

$$q_N(L_{DD}) = \left[1 - \left(\frac{L_{DD}(t) - L_{N,min}}{L_{N,ts} - L_{N,min}}\right)^{q_{N,l}}\right] \cdot (1 - q_{N,e}) \cdot \max\left\{\frac{N(t) - N_e}{N_{ts} - N_e}, 0\right\} \quad (28)$$

where:

- $L_{N,min}$: daylight duration of the shortest day of the year (hours),
- $L_{N,ts}$: daylight duration of the day of senescence onset (hours),
- $q_{N,l}$: leaf ageing parameter,
- $q_{N,e}$: fraction of evergreen biomass within the N vegetation compartment, considering that most of the biomass consists of trunks, branches, and twigs, and that the majority of species in the study area are evergreen.
- N_e: biomass of the evergreen non-host shrubs and trees,
- N_{ts}: N biomass at the time of onset of senescence of the current year.

This formulation prevents evergreen biomass from reduction during senescence, specifically, when the current biomass N equals N_e, senescence ceases. The values of the parameters of Eqs. (26)–(28) are reported in Tables S1 and S3 of Supplementary Material.

2.4.3. *Reservoir shrubs and trees* (R_S *and* R_I)

The growth and senescence dynamics of susceptible (R_S) and infected (R_I) reservoir compartments defined in Eqs. (1c) and (1d) are governed by a logistic growth function ($g_R(D_{OY}, T_{AH}, L_{DD}, R_S, R_I)$), a senescence function ($q_R(L_{DD})$). The biomass growth rate ($g_R(D_{OY}, T_{AH}, L_{DD}, R_S, R_I)$) is modelled using the same function as described in Eq. (26):

$$g_R(D_{OY}, T_{AH}, L_{DD}, R_S, R_I) = g_{R,T}(D_{OY}, T_{AH}, L_{DD}) \cdot \left(1 - \frac{R_S(t) + R_I(t)}{K_R}\right), \quad (29)$$

where $g_{R,T}(D_{OY}, T_{AH}, L_{DD})$ is defined analogously to Eq. (27).

The senescence rate function $q_R(D_{DL})$ is modeled using the same function described in Eq. (28):

$$q_R(L_{DD}) = \left[1 - \left(\frac{L_{DD}(t) - L_{R,min}}{L_{R,ts} - L_{R,min}}\right)^{q_{R,l}}\right] \cdot (1 - q_{R,e}) \cdot \max\left\{\frac{R_S(t) + R_I(t) - R_e}{R_{ts} - R_e}, 0\right\} \quad (30)$$

where:

- R_e: biomass of the evergreen reservoir shrubs and trees (kg ha^{-1}),
- R_{ts}: total biomass of reservoir vegetation at the time of senescence onset (kg ha^{-1}),
- $L_{R,min}$, $L_{R,ts}$, $q_{R,l}$, and $q_{R,e}$ are set equal to the corresponding parameters defined for non-host shrubs and trees (N) in Section 2.4.2.

2.5. *Case study*

The case study was designed to represent the outbreak of *Xf* in olive groves of Apulia, southern Italy. To this end, the model (Eq. (1)) was applied to capture the dynamics of disease dynamics in naturally infected olive trees from 16 olive groves in the *Xf*-infected area of Lecce province, in which qPCR had confirmed the presence of *Xf* (Zarco-Tejada et al., 2018, 2021). Between 2016 and 2019, a total of 3099 olive trees were monitored for 1 to 3 years, with disease severity visually assessed between two and nine times per tree. Most groves consisted of old trees (over 50 years old) of the highly susceptible cultivars Ogliarola Salentina and Cellina di Nardò, within a landscape dominated by olive groves.

The study area is characterized by a Mediterranean climate (Cs according to the Köppen-Geiger classification), with mild, wet winters and hot-dry summers (Kottek et al., 2006). Meteorological data were retrieved from Visual Crossing Corporation (2025) and interpolated using the Inverse Distance Weighting (IDW) method implemented in the *gstat* R package (Pebesma, 2004). The dataset included hourly temperature, daily precipitation (Figs. S1 and S2, Supplementary Material), solar radiation, and daylight duration.

2.6. *Model calibration and validation*

The eco-epidemiological model was calibrated using disease severity data from five olive groves. Calibration focused on two key parameters: host susceptibility to *Xf* infection ($i_{C,sp}$ and $i_{R,sp}$, Eq. (13)) and the non-systemic infection recovery rate ($r_{C,np}$ and $r_{R,np}$, Eq. (23)), both assumed equal for olive trees and reservoir shrubs and trees. The landscape composition of each monitored grove was reproduced in simulations by defining olive tree density and the carrying capacities of non-host shrubs and trees (K_N) and reservoir shrubs and trees (K_R) based on high-resolution satellite imagery (Google Earth Pro, Google Inc.© 2024) and biomass estimates (Pasalodos-Tato et al., 2015). Initial conditions were set to reflect realistic field situations, including herbaceous biomass, woody vegetation cover, reservoir infection levels, and vector population density. A detailed description of parameter values and

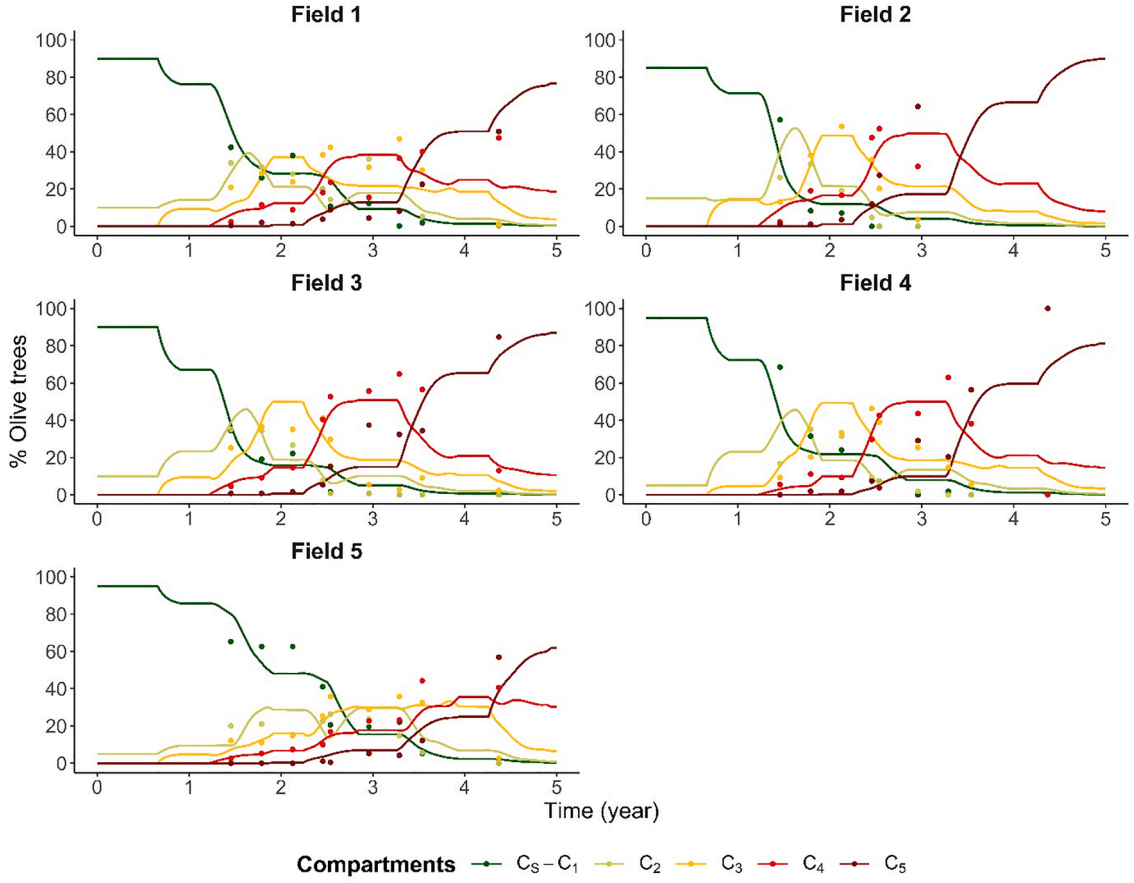

Fig. 4. Trends of infection over five years (2015–2019) at the five calibration sites. Lines represent the simulated percentage of olive trees in each disease stage, while points indicate observed field data in the *Xf*-infected area of Lecce province (Zarco-Tejada et al., 2018, 2021). C_S-C_1: Non-symptomatic olives; C_2: (0 %, 25 %] canopy with desiccated branches; C_3: (25 %, 50 %]; C_4: (50 %, 75 %]; and C_5: (75 %, 100 %] canopy with desiccated branches or fully desiccated trees.

initial conditions is provided in Section S2 (Supplementary Material).

Simulations were initialized starting from January 1, 2015, as the baseline date for the model to account for transmission history and disease progression. They were run over a 5-year period to capture long-term epidemic dynamics. Model calibration was performed by minimizing the error between simulated and observed cumulative numbers of olive trees in each disease stage, with the best-fitting parameter set selected for calibration. Root mean square error (RMSE) values between simulated and observed percentages of olive trees across disease stages are reported.

The model was validated based on 11 additional olive groves containing between two and nine evaluations per tree. Acknowledging that some datasets provide limited temporal resolution (two–three time points), they have been included in the evaluation because they still capture the overall trajectory of disease progression during the observation window and therefore allowed to test model behaviour.

3. Results

3.1. Model calibration

The model was calibrated to accurately reproduce the observed dynamics of disease progression across the study fields. The susceptibility of olive trees ($i_{C,sp}$) and reservoir shrubs and trees ($i_{R,sp}$) to *Xf* infection resulted from model calibration was estimated at 0.01, indicating a 100-fold reduction in the infection rate of individual infected vectors estimated in the model. The non-systemic disease recovery rate of newly infected olive trees ($r_{C,np}$) was set at 2.09×10^{-4} h^{-1}, meaning that up to 0.5 % of early-stage infections (within disease stage C_0) failed to become established in host every day. This recovery rate was also applied to reservoir shrubs and trees ($r_{R,np}$).

Despite the complexity of the system, the simulations successfully captured the overall trends, reproducing both the timing of increases and subsequent declines in the proportions of trees at each disease stage (Fig. 4). Calibration performance, expressed as the average RMSE between simulated and observed percentages of olive trees among calibration fields, was estimated as 10.36 %, ranging from 8.49 % in field 5 to 12.46 % in field 4, indicating satisfactory model estimates. Nonetheless, the model was less effective in reproducing certain complex patterns observed in the field, such as multi-peaked dynamics across years (e.g., stages C_2 and C_3 in fields 1 and 5) and rapid, large fluctuations in the proportion of trees within disease stages. These discrepancies are partly attributable to sampling variability, particularly the inherent uncertainty associated with visual classification of disease stages over time.

3.2. Model validation

The simulated epidemiological dynamics of olive trees showed good agreement with the observed data across most validation fields (Fig. 5). Similar to the calibration fields, the model effectively reproduced the overall patterns of disease progression across all stages, capturing the timing and general trends of increase and decrease in the proportions of trees at each disease stage. Accuracy was generally higher for non-symptomatic trees (C_S-C_1) and fully desiccated trees (C_5), while the intermediate stages were less precisely reproduced, reflecting more variable dynamics in the field. The average RMSE across validation fields was 10.98 %, with values ranging from 3.59 % in field 11 to 16.25

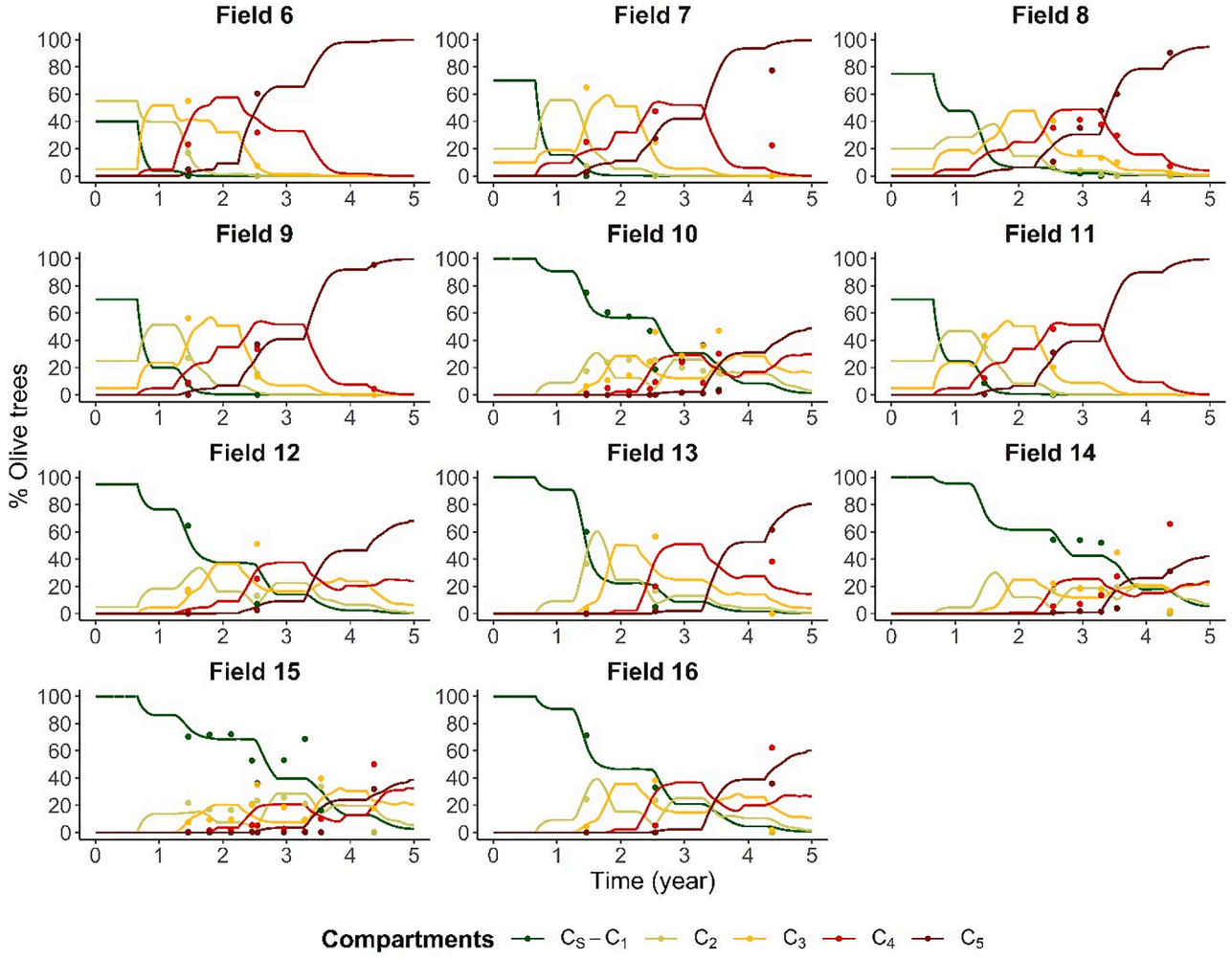

Fig. 5. Trends of infection over five years (2015–2019) at the validation sites. Lines represent the simulated percentage of olive trees in each disease stage, while points indicate observed field data in the *Xf*-infected area of Lecce province (Zarco-Tejada et al., 2018, 2021). C_S-C_1: Non-symptomatic olives; C_2: (0, 25 %] canopy with desiccated branches; C_3: (25 %, 50 %]; C_4: (50 %, 75 %]; and C_5: (75 %, 100 %] canopy with desiccated branches or fully desiccated trees.

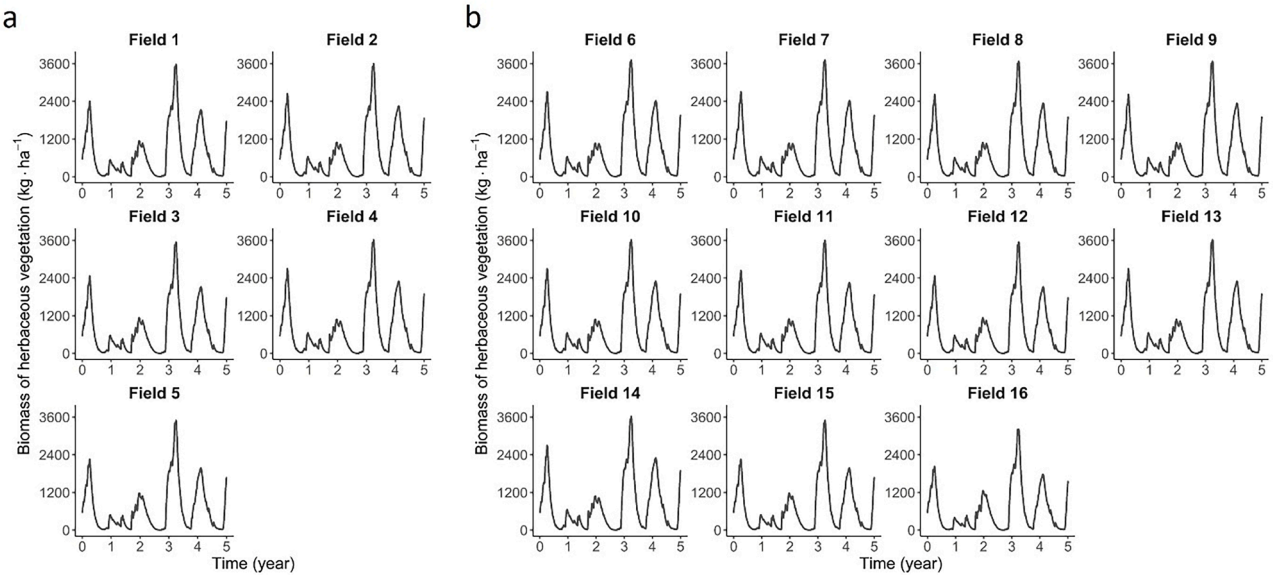

Fig. 6. Simulated herbaceous biomass dynamics (H) (kg ha^{-1}) over five-year period (2015–2019) in olive groves used for model calibration (a) and validation (b) in the Apulia region, Italy.

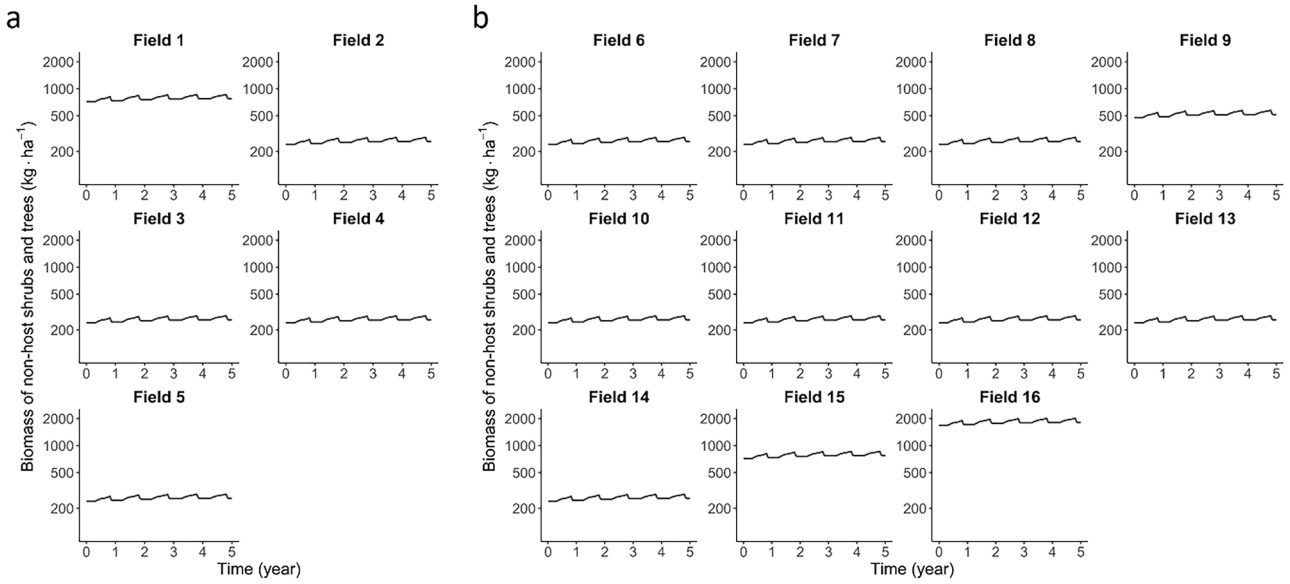

Fig. 7. Simulated biomass dynamics of non-host shrubs and trees (N) (kg ha^{-1}) over five-year period (2015–2019) in olive groves used for model calibration (a) and validation (b) in the Apulia region, Italy.

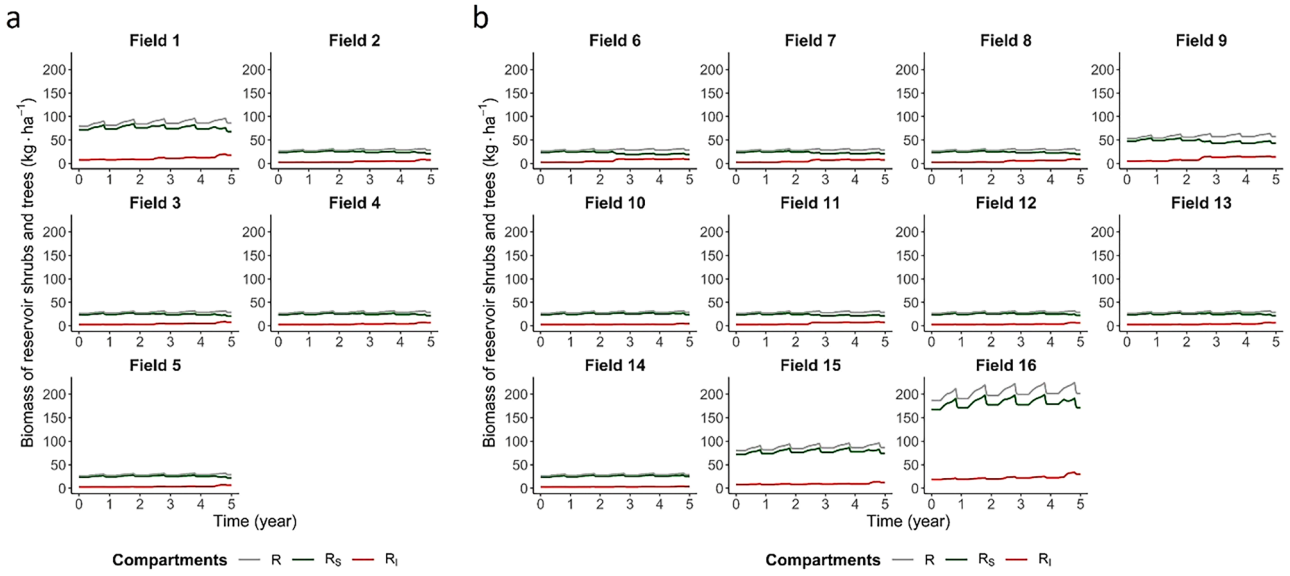

Fig. 8. Simulated biomass dynamics of susceptible (R_S), infected (R_I) and total reservoir shrubs and trees (R) (kg ha^{-1}) over five-year period (2015–2019) in olive groves used for model calibration (a) and validation (b) in the Apulia region, Italy.

% in field 14, highlighting some variability in model performance across validation sites.

3.3. Simulated dynamics across all olive groves

3.3.1. Herbaceous vegetation (H) and non-host shrubs and trees (N)

The H biomass showed a consistent temporal pattern across all olive groves during the 5-year simulation (Fig. 6). Significant growth occurred from late autumn to mid-spring, followed by a marked decline in late spring and summer. Across all fields, the mean H biomass (± standard error) ranged from a maximum of 3584.83 ± 29.93 kg ha^{-1} in the spring of the fourth year to a minimum of 5.56 ± 0.02 kg ha^{-1} in the summer of the fourth year. Notably, lower biomass peaks were observed during the winter and spring of the second year, with an average maximum of 627.55 ± 6.65 kg ha^{-1}, due to the reduced precipitation that constrained the growth rate.

The biomass of N presented a consistent temporal pattern across all olive groves during the five-year simulation (Fig. 7), gradually progressing towards the carrying capacity defined for each field. Periods of highest biomass growth were observed during the period from spring to early summer and again in early autumn, when temperature conditions were close to the estimated optimum temperature for woody biomass growth (i.e., 17.5 °C).

3.3.2. Reservoir shrubs and trees

The temporal dynamics of total reservoir plant biomass ($R_S + R_I$) followed a pattern similar to that observed for N (Fig. 8). Throughout the simulation period, the biomass of R_I plants steadily increased in all fields, with a more pronounced rise during the second half of the simulation. By the end of the simulation period, the average percentage of R_I biomass reached 23.08 % ± 1.46 %, with highest percentage recorded in field 6 (31.83 %), while field 14 presented the lowest value

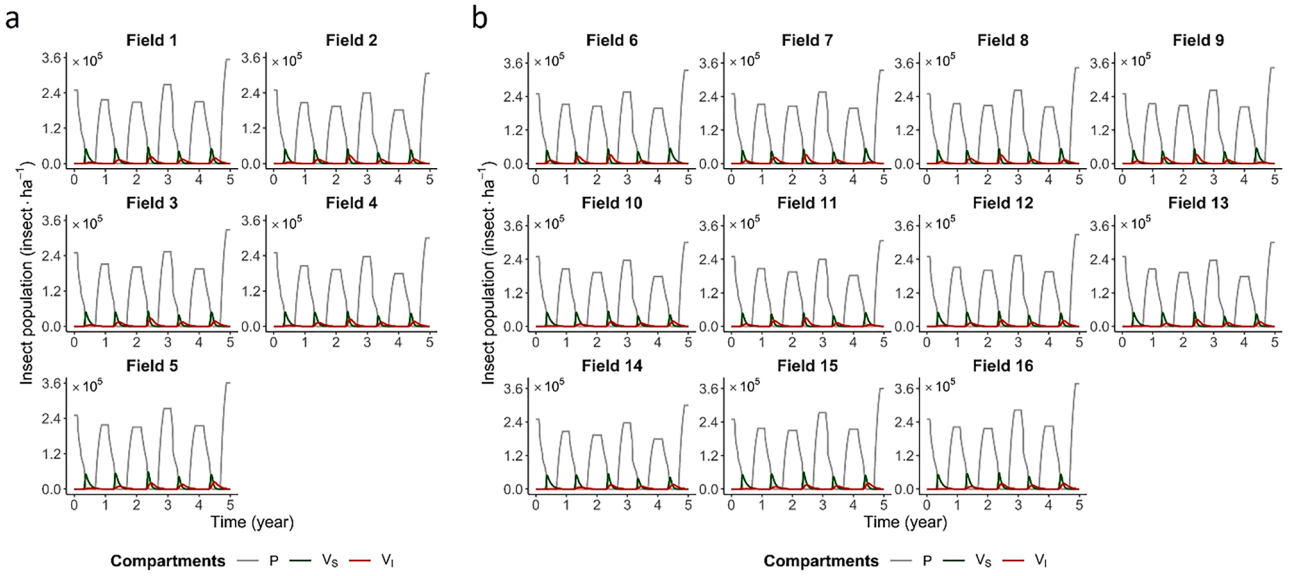

Fig. 9. Simulated number of preimaginal stage (P), and susceptible (V_S) and infected (V_I) adult stages of *Philaenus spumarius* over five-year period (2015–2019) in olive groves used for model calibration (a) and validation (b) in the Apulia region, Italy.

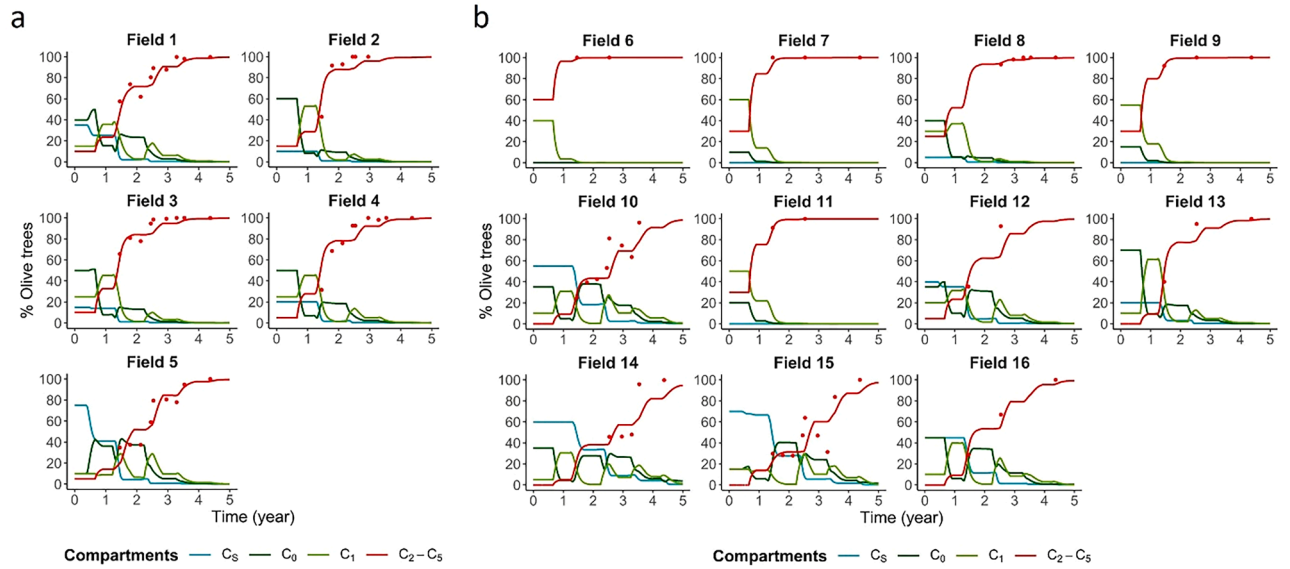

Fig. 10. Percentage (%) of olive trees in each disease stage over five-year period (2015–2019) in olive groves used for model calibration (a) and validation (b) in the Apulia region, Italy. Lines represent the simulated dynamics, while points represent the observed dynamics from field data in the *Xf*-infected area of Lecce province. C_S: non-infected olive trees; C_0: latent trees; C_1: infectious asymptomatic trees; and C_2-C_5: Symptomatic trees.

(13.47 %), starting from an initial R_I percentage of approximately 10 % at all fields.

3.3.3. Insect vector

P. spumarius showed marked interannual variability in population abundance across all fields during the 5-year simulation period (Fig. 9). The temporal dynamics of insect population followed a similar pattern among all olive groves. The infection prevalence in vector population varied notably across fields and years. Within each year, the simulated percentage of V_I gradually increased until mid-November, marking the end of adult longevity. In most fields, the lowest annual peak of V_I prevalence occurred in the first simulation year, with values ranging from 23.44 % in field 14 to 78.01 % in field 2, and highest prevalence typically observed between the third and fifth years, with peaks reaching approximately 100 %. These peaks coincided with periods of higher prevalence of infective olive trees at intermediate disease stages, representing still suitable hosts for the vectors and thus more likely to transmit the pathogen (Fig. 1).

3.3.4. Epidemiological dynamic in olive trees

In most fields, the majority of trees were either susceptible (C_S) or in the early stages of infection (C_0 and C_1) during the first simulation year, indicating the early phases of *Xf* outbreaks (Figs. 4 and 5). In these fields, approximately half of trees transitioned to symptomatic stages by the end of the second year and the third year, with full prevalence of symptomatic trees generally reached by the fourth or fifth year. In contrast, fields with advanced initial infection (i.e., 6, 7, 9, and 11) showed a rapid decline in non-symptomatic stages toward the end of the first year, with the entire tree population becoming symptomatic by the second year of simulation (Figs. 4 and 5). The dynamics of stages C_S, C_0,

and C_1, along with the aggregated symptomatic stage dynamics, are shown in Fig. 10.

The estimated curves for symptomatic stages displayed a consistent progression within each field. The dynamics of each stage followed those of the preceding stage, with a temporal offset reflecting the stage-specific delay and the seasonal interruption of disease progression during winter months. Bacterial mortality ($b_{m\ sp}^{C_i}$) had a minor influence on overall disease dynamics, as extreme temperatures were rarely reached within the climatic range for the simulation study.

Progression to the final disease stage (C_5) typically began at the start of the third simulation year, with a marked increase during the fourth year. Significant accumulation of trees in stage C_5 occurred approximately 2.5 years after the first appearance of symptoms. By the end of simulation period, the proportion of trees in stage C_5 ranged from 38.60 % to 94.78 %.

4. Discussion

The eco-epidemiological modelling framework developed in this study effectively captures the key biological processes and abiotic drivers underlying the dynamics of the *Xf* pathosystem in olive agroecosystems. A major advance over previous epidemiological models (e.g., Brunetti et al., 2020; White et al., 2020; Giménez-Romero et al., 2023) lies in the physiologically-based mechanistic representation of disease progression in olive trees, structured into compartments corresponding to distinct infection stages and symptom severity levels. Transitions between stages are described by physiologically based processes linked to within-host bacterial dynamics and symptom development, modulated by biotic factors such as host phenology, susceptibility, and superinfection events, as well as abiotic variables including temperature and soil moisture. This contrasts with former approaches that relied largely on fixed progression rates, thereby limiting their capacity to reflect local biotic and abiotic variability (but see Giménez-Romero et al., 2022). While Gilioli et al. (2023) introduced seasonal variation in bacterial growth through discrete seasonal regimes, the present framework models these effects using continuous, non-linear functions explicitly coupled to climatic conditions and plant phenology, enhancing biological realism and generalizability. In addition, the explicit representation of a structured vector population dynamic and the seasonal patterns of population abundance and interaction with host plants, further advances previous formulations that neglected vector demography (White et al., 2020) or relied on simplified population structures or seasonal forcing functions (Brunetti et al., 2020; Gilioli et al., 2023; Giménez-Romero et al., 2023). Finally, the composite structure of the model enables explicit integration of multiple landscape components, allowing the exploration of heterogeneous agroecosystems.

Climatic conditions in southern Apulia, Italy, during the simulation period were characterized by warm-hot temperatures and mild winters, which are favourable for the development and persistence of *Xf* subsp. *pauca* infection in olive trees (EFSA PLH Panel, 2019; Godefroid et al., 2019). The consistently suitable temperatures from late spring through mid-autumn supported the effective establishment and rapid disease progression, while the absence of cold-induced mechanisms limited natural disease regression under the estimated model parameters. Future climate change scenarios are expected to increase the frequency and intensity of heat stress events, which may potentially reduce the environmental suitability of the region for *Xf* infection (Bosso et al., 2016; Giménez-Romero et al., 2022).

Symptom progression in olive trees was further influenced by seasonal water stress, particularly during summer months. Prolonged drought periods accelerated symptom expression, while increased rainfall and cooler temperatures during autumn tend to mitigate disease progression, consistent with previous findings (De Pascali et al., 2022; Wallis and Gorman, 2024). However, the role of water stress in disease dynamics remains unclear, as it may also affect bacterial proliferation and vector behaviour (Godefroid et al., 2019), warranting further investigation. During model parameterization, disease dynamics appeared more responsive to parameters governing temperature-dependent bacterial growth than to those associated with plant water stress, while parameters related to bacterial mortality and superinfection showed comparatively limited effects under the simulated conditions. These observations reflect qualitative model behaviour and do not represent a formal sensitivity analysis.

The average duration of the asymptomatic period in our model was consistent with empirical and model-based estimates of approximately 1 year (EFSA PLH Panel, 2019; Saponari et al., 2017). Model simulations estimated that disease progression from the initial phase of *Xf* outbreak to the point where the entire population exhibited maximum disease severity averaged approximately 5 years, aligning with estimates reported by White et al. (2020) and Giménez-Romero et al. (2023).

The results show that the abundance of infected adult vectors peaked during summer, in agreement with previous modelling studies (Gilioli et al., 2023; Giménez-Romero et al., 2023). The prevalence of infected vectors gradually increased until mid-November, often exceeding 90 % of the total vector population during most of the simulated years. Field observations, however, show more variable and non-linear seasonal patterns, with infection prevalence in vectors rarely surpassing 70 % (Ben Moussa et al., 2016; Cavalieri et al., 2019; Cornara et al., 2017). These differences may reflect influence of spatial and temporal heterogeneity in host plant infection, climate variability, and the seasonal movements of vector among host compartments, all of which can also affect the estimates of prevalence of infected vectors derived from field sampling.

Vector infectivity was highest when olive trees in intermediate disease stages were most prevalent, subsequently declining as trees advanced to severe disease stages, which are less attractive to vectors (Daugherty et al., 2011). This pattern has also been documented in Apulia in recent years (Bodino et al., 2023), where widespread tree desiccation and the introduction of resistant cultivars (characterized by lower bacterial loads even when infected) are believed to have contributed to declining vector infection rates. High vector infection levels observed in model simulations also reflect the predominance of susceptible olive trees in the simulated landscape, mirroring the typical host composition in the Apulian outbreak zone. The limited presence of non-host woody vegetation likely contributed to sustained transmission, highlighting the role of host plant composition in shaping epidemic dynamics (Cornara et al., 2018).

Reservoir shrubs and trees in the simulations exhibited a slow increase in infection prevalence over time, likely due to their lower abundance compared to other vegetation compartments. This resulted in reduced contact rates with infected vectors and limited transmission events. While their contribution to *Xf* spread appears marginal under the simulated conditions, further research is essential to clarify the role of reservoir shrubs and trees in *Xf* epidemiology. Specifically, experimental data on their transmission efficiency, latency period, and symptom expression are needed to better inform risk assessments and support effective management strategies.

Model parameterization presented several challenges due to the limited empirical data on the bioecological processes governing disease dynamics and vector dynamics. As a result, functions describing disease progression and regression, as well as vector population processes, were largely derived from biologically informed assumptions and sparse experimental evidence providing indirect guidance for parameter estimation, and will require further validation and refinement as additional data become available. Despite these constraints, the parametrization and calibration produced a coherent and biologically plausible parameter set, with simulated outputs consistent with field observations, and offers a structured framework that may guide future empirical and modelling efforts aimed at better characterizing these bioecological processes. However, both calibration and validation relied on data from

a geographically restricted area with relatively homogeneous environmental and landscape conditions. Initial distributions of disease stages were inferred due to the absence of field data, and vector populations were assumed uniform across sites, a reasonable assumption given the spatial proximity of fields and similar landscape contexts, but still a source of uncertainty. Model calibration and validation using independent datasets from other *Xf* outbreak regions in olive groves (e.g., Mallorca Island) will be essential to assess model generalizability under different environmental and climatic conditions.

Future enhancements could incorporate spatially explicit network modelling to more accurately capture landscape-level disease spread and the influence of management practices. Overall, this framework not only advances scientific understanding of Xf epidemiology but also directly supports decision-making for effective disease containment and sustainable management in affected olive-growing regions. This mechanistic, stage-structured model provides a valuable tool for both pest risk assessment (PRA) and integrated pest management (IPM). For PRA, it enables simulation of disease spread under varying environmental and host conditions, supporting risk evaluation and contingency planning. For IPM, it allows assessment of intervention strategies targeting different system components (i.e., trees, vectors, or reservoirs) by incorporating intervention-induced mortality or delay effects.

5. Conclusion

This study presents a physiologically based, mechanistic model that integrates host, pathogen, vector, and environmental processes to simulate the eco-epidemiological dynamics of *Xf* in olive systems. Model simulations closely reproduced observed durations of the asymptomatic phase and the time required to reach complete canopy desiccation, and highlighted the roles of seasonal vector dynamics, host plant preference, and landscape composition in shaping transmission patterns. By explicitly linking epidemiological processes to climatic and biological drivers, the framework advances previous modelling approaches and improves biological realism and applicability across environmental contexts. The model enables a more detailed and mechanistic exploration of how climate and landscape factors influence epidemic dynamics through their effects on multiple components of the pathosystem. These features make the model a useful operational tool for evaluating disease establishment risk and management scenarios, supporting pest risk assessment, surveillance design, and guide integrated management strategies for *Xf* outbreaks.

Consent to publish

All authors read and approved the manuscript.

Declaration of generative AI and AI-assisted technologies in the manuscript preparation process

During the preparation of this work, the authors used ChatGPT (version 5.2, OpenAI) for language revision, grammar and spelling correction, and general editing support. After using this tool, the authors carefully reviewed and edited the content as needed and take full responsibility for the content of the published article.

CRediT authorship contribution statement

Igor Daniel Weber: Writing – review & editing, Writing – original draft, Validation, Software, Methodology, Formal analysis, Data curation, Conceptualization. **Anna Simonetto:** Writing – review & editing, Validation, Software, Methodology, Formal analysis, Conceptualization. **Enrico Bertoldi:** Writing – review & editing, Software, Methodology, Formal analysis. **Paola Gervasio:** Writing – review & editing, Software, Methodology, Formal analysis. **Maria Saponari:** Writing – review & editing, Investigation, Conceptualization. **Crescenza Dongiovanni:** Writing – review & editing, Investigation. **Juan Antonio Navas-Cortés:** Writing – review & editing, Investigation, Conceptualization. **Gianni Gilioli:** Writing – review & editing, Supervision, Methodology, Funding acquisition, Formal analysis, Conceptualization.

Declaration of competing interest

The authors declare that they have no conflict of interest.

Acknowledgment

This work was funded by the European Union's Horizon Europe Research and Innovation Program (BeXyl grant 101060593).

Supplementary materials

Supplementary material associated with this article can be found, in the online version, at doi:10.1016/j.ecolmodel.2026.111546.

Data availability

The data will be available from the corresponding author upon reasonable request.

References

Allen, R.G., Pereira, L.S., Raes, D., Smith, M., 1998. Crop Evapotranspiration-Guidelines For Computing Crop Water Requirements-FAO Irrigation and Drainage Paper 56, 300. Fao, Rome. D05109.

Almeida, R.P.P., Wistrom, C., Hill, B.L., Hashim, J., Purcell, A.H., 2005. Vector transmission of *Xylella fastidiosa* to dormant grape. Plant Dis. 89 (4), 419–424. https://doi.org/10.1094/PD-89-0419.

Aniţa, S., Capasso, V., Scacchi, S., 2021. Controlling the spatial spread of a *Xylella* epidemic. Bull. Math. Biol. 83 (4), 32. https://doi.org/10.1007/s11538-021-00861-z.

Avosani, S., Franceschi, P., Ciolli, M., Verrastro, V., Mazzoni, V., 2021. Vibrational playbacks and microscopy to study the signalling behaviour and female physiology of *Philaenus spumarius*. J. App. Entomol. 145 (6), 518–529. https://doi.org/10.1111/jen.1287.

Ben Moussa, I.E., Mazzoni, V., Valentini, F., Yaseen, T., Lorusso, D., Speranza, S., Digiaro, M., Varvaro, L., Krugner, R., D'Onghia, A.M., 2016. Seasonal fluctuations of sap-feeding insect species infected by *Xylella fastidiosa* in Apulian olive groves of Southern Italy. J. Econ. Entomol. 109 (4), 1512–1518. https://doi.org/10.1093/jee/tow123.

Bodino, N., Demichelis, S., Simonetto, A., Volani, S., Saladini, M.A., Gilioli, G., Bosco, D., 2021. Phenology, seasonal abundance, and host-plant association of spittlebugs (Hemiptera: aphrophoridae) in vineyards of Northwestern Italy. Insects 12, 1012. https://doi.org/10.3390/insects12111012.

Bodino, N., Simonetto, A., Dongiovanni, C., Cavalieri, V., Di Carolo, M., Gilioli, G., Bosco, D., Saponari, M., 2023. Bioecological traits of spittlebugs and their implications for the epidemiology and control of the *Xylella fastidiosa* epidemic in Apulia. Sci. Rep. 13 (1), 13062. https://doi.org/10.1038/s41598-023-40084-5.

Bosso, L., Di Febbraro, M., Cristinzio, G., Zoina, A., Russo, D., 2016. Shedding light on the effects of climate change on the potential distribution of *xylella fastidiosa* in the Mediterranean basin. Biol. Invasions 18 (6), 1759–1768. https://doi.org/10.1007/s10530-016-1118-1.

Brunetti, M., Capasso, V., Montagna, M., Venturino, E., 2020. A mathematical model for *Xylella fastidiosa* epidemics in the Mediterranean regions. Promoting good agronomic practices for their effective control. Ecol. Modell. 432, 109204. https://doi.org/10.1016/j.ecolmodel.2020.109204.

Castellini, M., Stellacci, A.M., Mastrangelo, M., Caputo, F., Manici, L.M., 2020. Estimating the soil hydraulic functions of some olive orchards: soil management implications for water saving in soils of Salento Peninsula (Southern Italy). Agronomy 10 (2), 177. https://doi.org/10.3390/agronomy10020177.

Cavalieri, V., Altamura, G., Fumarola, G., di Carolo, M., Saponari, M., Cornara, D., Bosco, D., Dongiovanni, C., 2019. Transmission of *Xylella fastidiosa* subspecies pauca sequence type 53 by different insect species. Insects 10 (10), 324. https://doi.org/10.3390/insects10100324.

Cavalieri, V., Fasanelli, E., Furnari, G., Gibin, D., Gutierrez Linares, A., La Notte, P., Pasinato, L., Stancanelli, G., Delbianco, A., 2025. Update of the *Xylella* spp. host plant database – systematic literature search up to 30 June 2024. EFSA J. 23 (2), e9241. https://doi.org/10.2903/j.efsa.2025.9241.

Cendoya, M., Navarro-Quiles, A., López-Quílez, A., Vicent, A., Conesa, D., 2024. An individual-based spatial epidemiological model for the spread of plant diseases. J. Agric. Biol. Environ. Stat. https://doi.org/10.1007/s13253-024-00604-2.

Cornara, D., Saponari, M., Zeilinger, A.R., de Stradis, A., Boscia, D., Loconsole, G., Bosco, D., Martelli, G.P., Almeida, R.P.P., Porcelli, F., 2017. Spittlebugs as vectors of

Xylella fastidiosa in olive orchards in Italy. J. Pest Sci. 90 (2), 521–530. https://doi.org/10.1007/s10340-016-0793-0.
Cornara, D., Bosco, D., Fereres, A., 2018. *Philaenus spumarius*: when an old acquaintance becomes a new threat to European agriculture. J. Pest Sci. 91 (3), 957–972. https://doi.org/10.1007/s10340-018-0966-0.
Daugherty, M.P., Almeida, R.P.P., 2009. Estimating *Xylella fastidiosa* transmission parameters: decoupling sharpshooter number and feeding period. Entomol. Exp. Appl. 132, 84–92. https://doi.org/10.1111/j.1570-7458.2009.00868.x.
Daugherty, M.P., Rashed, A., Almeida, R.P.P., Perring, T.M., 2011. Vector preference for hosts differing in infection status: sharpshooter movement and *xylella fastidiosa* transmission. Ecol. Entomol. 36, 654–662. https://doi.org/10.1111/j.1365-2311.2011.01309.x.
De Pascali, M., Vergine, M., Negro, C., Greco, D., Vita, F., Sabella, E., De Bellis, L., Luvisi, A., 2022. *Xylella fastidiosa* and drought stress in olive trees: a complex relationship mediated by soluble sugars. Biol 11 (1), 112. https://doi.org/10.3390/biology11010112.
Didevarasl, A., Costa Saura, J.M., Spano, D., Deiana, P., Snyder, R.L., Mulas, M., Nieddu, G., Zelasco, S., Santona, M., Trabucco, A., 2023. Modeling phenological phases across olive cultivars in the Mediterranean. Plants 12 (18), 3181. https://doi.org/10.3390/plants12183181.
Di Serio, F., Bodino, N., Cavalieri, V., 2019. Collection of Data and Information on Biology and Control of Vectors of *Xylella fastidiosa*, 16. EFSA Supporting Publications, p. 1628E. https://doi.org/10.2903/sp.efsa.2019.EN-1628. EN-1628.
Dombrowski, O., Brogi, C., Hendricks Franssen, H.-J., Zanotelli, D., Bogena, H., 2022. CLM5-FruitTree: a new sub-model for deciduous fruit trees in the Community Land Model (CLM5). Geosci. Model Dev. 15 (13), 5167–5193. https://doi.org/10.5194/gmd-15-5167-2022.
Dufrêne, E., Davi, H., François, C., Le Maire, G., Le Dantec, V., Granier, A., 2005. Modelling carbon and water cycles in a beech forest. Part I: model description and uncertainty analysis on modelled NEE. Ecol. Modell. 185 (2–4), 407–436. https://doi.org/10.1016/j.ecolmodel.2005.01.004.
EFSA Panel on Plant Health (PLH), 2019. Update of the scientific opinion on the risks to plant health posed by *Xylella fastidiosa* in the EU territory. EFSA J. 17 (5), 5665. https://doi.org/10.2903/j.efsa.2019.5665.
Feil, H., Purcell, A.H., 2001. Temperature-dependent growth and survival of *Xylella fastidiosa* in vitro and in potted grapevines. Plant Dis. 85, 1230–1234.
Fierro, A., Liccardo, A., Porcelli, F., 2019. A lattice model to manage the vector and the infection of the *Xylella fastidiosa* on olive trees. Sci. Rep. 9 (1), 8723. https://doi.org/10.1038/s41598-019-44997-4.
Gambella, F., Bianchini, L., Cecchini, M., Egidi, G., Ferrara, A., Salvati, L., Colantoni, A., Morea, D., 2021. Moving toward the north? The spatial shift of olive groves in Italy. Agric. Econ. – Czech. 67, 129–135. https://doi.org/10.17221/467/2020-AGRICECON.
Gilioli, G., Pasquali, S., Marchesini, E., 2016. A modelling framework for pest population dynamics and management: an application to the grape berry moth. Ecol. Modell. 320, 348–357. https://doi.org/10.1016/j.ecolmodel.2015.10.018.
Gilioli, G., Simonetto, A., Colturato, M., Bazarra, N., Fernández, J.R., Naso, M.G., Boscia, D., Bosco, D., Dongiovanni, C., Maiorano, A., Mosbach-Schulz, O., Navas Cortés, J.A., Saponari, M., 2023. An eco-epidemiological model supporting rational disease management of *Xylella fastidiosa*. An application to the outbreak in Apulia (Italy). Ecol. Modell. 476, 110226. https://doi.org/10.1016/j.ecolmodel.2022.110226.
Gilioli, G., Simonetto, A., Weber, I.D., Gervasio, P., Sperandio, G., Bosco, D., Bodino, N., Dongiovanni, C., Di Carolo, M., Cavalieri, V., Saponari, M., Boscia, D., 2024. A model for predicting the phenology of *Philaenus spumarius*. Sci. Rep. 14 (1), 8137. https://doi.org/10.1038/s41598-024-58798-x.
Giménez-Romero, A., Galván, J., Montesinos, M., Bauzà, J., Godefroid, M., Fereres, A., Ramasco, J.J., Matías, M.A., Moralejo, E., 2022. Global predictions for the risk of establishment of Pierce's disease of grapevines. Commun. Biol. 5 (1), 1389. https://doi.org/10.1038/s42003-022-04358-w.
Giménez-Romero, A., Moralejo, E., Matías, M.A., 2023. A compartmental model for *Xylella fastidiosa* diseases with explicit vector seasonal dynamics. Phytopathology 113, 1686–1696. https://doi.org/10.1094/PHYTO-11-22-0428-V.
Godefroid, M., Cruaud, A., Streito, J.C., Rasplus, J.Y., Rossi, J.P., 2019. *Xylella fastidiosa*: climate suitability of European continent. Sci. Rep. 9, 8844. https://doi.org/10.1038/s41598-019-45365-y.
Hill, B.L., Purcell, A.H., 1997. Populations of *xylella fastidiosa* in plants required for transmission by an efficient vector. Phytopathology 87, 1197–1201. https://doi.org/10.1094/PHYTO.1997.87.12.1197.
Hornero, A., Hernández-Clemente, R., North, P.R.J., Beck, P.S.A., Boscia, D., Navas-Cortes, J.A., Zarco-Tejada, P.J., 2020. Monitoring the incidence of *Xylella fastidiosa* infection in olive orchards using ground-based evaluations, airborne imaging spectroscopy and Sentinel-2 time series through 3-D radiative transfer modelling. Remote Sens. Environ. 236, 111480. https://doi.org/10.1016/j.rse.2019.111480.
Jeger, M., Bragard, C., 2019. The epidemiology of *Xylella fastidiosa*: a perspective on current knowledge and framework to investigate plant host–vector–pathogen interactions. Phytopathology 109 (2), 200–210. https://doi.org/10.1094/PHYTO-07-18-0239-FI.
Jeong, S.-J., Medvigy, D., 2014. Macroscale prediction of autumn leaf coloration throughout the continental United States. Glob. Ecol. Biogeogr. 23 (11), 1245–1254. https://doi.org/10.1111/geb.12206.
Kottek, M., Grieser, J., Beck, C., Rudolf, B., Rubel, F., 2006. World Map of the Köppen–Geiger climate classification updated. Meteorol. Z. 15, 259–263. https://doi.org/10.1127/0941-2948/2006/0130.
Lieth, J.H., Meyer, M.M., Yeo, K.-H., Kirkpatrick, B.C., 2011. Modeling cold curing of Pierce's disease in *Vitis vinifera* 'Pinot Noir' and 'Cabernet Sauvignon' Grapevines in California. Phytopathol 101 (12), 1492–1500. https://doi.org/10.1094/PHYTO-08-10-0207.
Liu, Q., Piao, S., Campioli, M., Gao, M., Fu, Y.H., Wang, K., He, Y., Li, X., Janssens, I.A., 2020. Modeling leaf senescence of deciduous tree species in Europe. Glob. Change Biol. 26 (7), 4104–4118. https://doi.org/10.1111/gcb.15132.
López-Bernal, Á., García-Tejera, O., Testi, L., Orgaz, F., Villalobos, F.J., 2020. Studying and modelling winter dormancy in olive trees. Agric. For. Meteorol. 280, 107776. https://doi.org/10.1016/j.agrformet.2019.107776.
Martin, O., Fernandez-Diclo, Y., Coville, J., Soubeyrand, S., 2021. Equilibrium and sensitivity analysis of a spatio-temporal host–vector epidemic model. Nonlinear Anal. Real World Appl. 57, 103194. https://doi.org/10.1016/j.nonrwa.2020.103194.
McCall, D.G., Bishop-Hurley, G.J., 2003. A pasture growth model for use in a whole-farm dairy production model. Agric. Syst. 76 (3), 1183–1205. https://doi.org/10.1016/S0308-521X(02)00104-X.
Morente, M., Cornara, D., Moreno, A., Fereres, A., 2021. Parapause breakage as a key step for the continuous indoor rearing of *Philaenus spumarius*. J. Appl. Entomol. 145 (10), 1062–1067. https://doi.org/10.1111/jen.12931.
Pasalodos-Tato, M., Ruiz-Peinado, R., del Río, M., Montero, G., 2015. Shrub biomass accumulation and growth rate models to quantify carbon stocks and fluxes for the Mediterranean region. Eur. J. For. Res. 134 (3), 537–553. https://doi.org/10.1007/s10342-015-0870-6.
Pebesma, E., 2004. Multivariable geostatistics in S: the gstat package. Comput. Geosci. 30 (7), 683–691. https://doi.org/10.1016/j.cageo.2004.03.012.
Quarteroni, A., Saleri, F., Gervasio, P., 2014. Scientific Computing with MATLAB and Octave. Springer Berlin, Heidelberg.
Rapicavoli, J., Ingel, B., Blanco-Ulate, B., Cantu, D., Roper, C., 2018. *Xylella fastidiosa*: an examination of a re-emerging plant pathogen. Mol. Plant. Pathol. 19 (4), 786–800. https://doi.org/10.1111/mpp.12585.
Romera, A.J., McCall, D.G., Lee, J.M., Agnusdei, M.G., 2009. Improving the McCall herbage growth model. N. Z. J. Agric. Res. 52 (4), 477–494. https://doi.org/10.1080/00288230909510529.
Rossi, S., Deslauriers, A., Anfodillo, T., Carraro, V., 2007. Evidence of threshold temperatures for xylogenesis in conifers at high altitudes. Oecologia 152 (1), 1–12. https://doi.org/10.1007/s00442-006-0625-7.
Saponari, M., Boscia, D., Nigro, F., Martelli, G.P., 2013. Identification of DNA sequences related to *Xylella fastidiosa* in oleander, almond and olive trees exhibiting leaf scorch symptoms in Apulia (Southern Italy). Disease note. J. Plant Pathol. 94, 688.
Saponari, M., Boscia, D., Altamura, G., Loconsole, G., Zicca, S., D'Attoma, G., Morelli, M., Palmisano, F., Saponari, A., Tavano, D., Savino, V.N., Dongiovanni, C., Martelli, G. P., 2017. Isolation and pathogenicity of *Xylella fastidiosa* associated to the olive quick decline syndrome in southern Italy. Sci. Rep. 7 (1), 17723. https://doi.org/10.1038/s41598-017-17957-z.
Saponari, M., Giampetruzzi, A., Loconsole, G., Boscia, D., Saldarelli, P., 2019. *Xylella fastidiosa* in Olive in Apulia: where we stand. Phytopathology® 109 (2), 175–186. https://doi.org/10.1094/PHYTO-08-18-0319-FI.
Schneider, K., Van der Werf, W., Cendoya, M., Mourits, M., Navas-Cortés, J.A., Vicent, A., Oude Lansink, A., 2020. Impact of *xylella fastidiosa* subspecies *pauca* in European olives. Proc. Nat. Acad. Sci. 117 (17), 9250–9259. https://doi.org/10.1073/pnas.1912206117.
Sicard, A., Zeilinger, A.R., Vanhove, M., Schartel, T.E., Beal, D.J., Daugherty, M.P., Almeida, R.P.P., 2018. *Xylella fastidiosa*: insights into an emerging plant pathogen. Annu. Rev. Phytopathol. 56, 181–202. https://doi.org/10.1146/annurev-phyto-080417-045849.
Silva, S.E., Rodrigues, A.S.B., Marabuto, E., Yurtsever, S., Borges, P.A.V., Quartau, J.A., Paulo, O.S., Seabra, S.G., 2015. Differential survival and reproduction in colour forms of *Philaenus spumarius* give new insights to the study of its balanced polymorphism. Ecol. Entomol. 40 (6), 759–766. https://doi.org/10.1111/een.12252.
Soubeyrand, S., de Jerphanion, P., Martin, O., Saussac, M., Manceau, C., Hendrikx, P., Lannou, C., 2018. Inferring pathogen dynamics from temporal count data: the emergence of *Xylella fastidiosa* in France is probably not recent. New Phytol. 219 (2), 824–836. https://doi.org/10.1111/nph.15177.
Sun, Q., Sun, Y., Walker, M.A., Labavitch, J.M., 2013. Vascular occlusions in grapevines with Pierce's disease make disease symptom development worse. Plant Physiol. 161 (3), 1529–1541. https://doi.org/10.1104/pp.112.208157.
Visual Crossing Corporation, 2025. Visual Crossing Weather. https://www.visualcrossing.com/ (accessed 10 February 2025).
Wallis, C.M., Gorman, Z., 2024. Pre-inoculation water deficit effects on grapevine physiology, *Xylella fastidiosa* titers, and Pierce's disease progression. BMC Res. Notes 17 (1), 119. https://doi.org/10.1186/s13104-024-06780-1.
White, S.M., Navas-Cortés, J.A., Bullock, J.M., Boscia, D., Chapman, D.S., 2020. Estimating the epidemiology of emerging *Xylella fastidiosa* outbreaks in olives. Plant Pathol. 69, 1403–1413. https://doi.org/10.1111/ppa.13238ppa.13238.
Witsack, W., 1973. Experimental and ecological investigations on forms of dormancy in homoptera-cicadina (Auchenorrhyncha). 2. On ovarian parapause and obligatory embryonic diapause in *Philaenus spumarius* (L.) (Aphrophoridae). Zool. Jahrb. Abt. Syst. Okol. Geogr. Tiere 100, 517–562.
Yan, W., Wallace, D.H., Ross, J., 1996. A model of photoperiod x temperature interaction effects on plant development. Crit. Rev. Plant Sci. 15, 63–96. https://doi.org/10.1080/07352689609701936.

Yurtsever, S., 2000. On the polymorphic meadow spittlebug, *Philaenus spumarius* (L.) (Homoptera: cercopidae). Turk. J. Zool. 24, 447–459.

Zarco-Tejada, P.J., Camino, C., Beck, P.S.A., Calderón, R., Hornero, A., Hernández-Clemente, R., Kattenborn, T., Montes-Borrego, M., Susca, L., Morelli, M., González-Dugo, V., Navas-Cortés, J.A., 2018. Previsual symptoms of *Xylella fastidiosa* infection revealed in spectral plant-trait alterations. Nat. Plants 4 (7), 432–439. https://doi.org/10.1038/s41477-018-0189-7.

Zarco-Tejada, P.J., Poblete, T., Camino, C., Gonzalez-Dugo, V., Calderon, R., Hornero, A., Hernandez-Clemente, R., Román-Écija, M., Velasco-Amo, M.P., Landa, B.B., Beck, P. S.A., Saponari, M., Boscia, D., Navas-Cortes, J.A., 2021. Divergent abiotic spectral pathways unravel pathogen stress signals across species. Nat. Commun. 12 (1), 6088. https://doi.org/10.1038/s41467-021-26335-3.